Research Paper

THEMED ISSUE: Different Personalities of Granites and Rhyolites: Silicic Magmas from the Lower Crust to the Surface

GEOSPHERE

GEOSPHERE, v. 17, no. 2

https://doi.org/10.1130/GES02286.1

13 figures; 3 tables; 1 set of supplemental files

CORRESPONDENCE: loppenheim@fullerton.edu

CITATION: Oppenheim, L.F., Memeti, V., Barnes, C.G., Chambers, M., Krause, J., and Esposito, R., 2021, Feldspar recycling across magma mush bodies during the voluminous Half Dome and Cathedral Peak stages of the Tuolumne intrusive complex, Yosemite National Park, California, USA: Geosphere, v. 17, no. 2, p. 322–351, https://doi.org/10.1130/GES02286.1.

Science Editor: Shanaka de Silva
Guest Associate Editor: Jonathan Miller

Received 20 May 2020
Revision received 3 September 2020
Accepted 10 November 2020

Published online 21 January 2021

Feldspar recycling across magma mush bodies during the voluminous Half Dome and Cathedral Peak stages of the Tuolumne intrusive complex, Yosemite National Park, California, USA

Louis F. Oppenheim[1], Valbone Memeti[1], Calvin G. Barnes[2], Melissa Chambers[1], Joachim Krause[3], and Rosario Esposito[4]

[1]Department of Geological Sciences, California State University, Fullerton, California 92831, USA
[2]Department of Geosciences, Texas Tech University, Lubbock, Texas 07409-1053, USA
[3]Helmholtz-Zentrum Dresden-Rossendorf, Helmholtz Institute Freiberg for Resource Technology, Chemnitzer Straße 40, 09599 Freiberg, Germany
[4]Department of Earth, Planetary, and Space Sciences, University of California, Los Angeles, California 90095-1567, USA

ABSTRACT

Incremental pluton growth can produce sheeted complexes with no magma-magma interaction or large, dynamic magma bodies communicating via crystal and melt exchanges, depending on pulse size and frequency of intrusions. Determining the degree and spatial extent of crystal-melt exchange along and away from plutonic contacts at or near the emplacement level, such as in the large, long-lived Tuolumne intrusive complex (TIC) in California, sheds light onto the process and evolution of incremental growth.

This study used field mapping and petrographic and geochemical analysis of plagioclase and K-feldspar populations in the equigranular Half Dome (eHD), porphyritic Half Dome (pHD), and Cathedral Peak (CP) Granodiorites of the southeastern section of the TIC to determine the presence and/or extent of feldspar recycling at interunit contacts. Our results suggest that contacts between major units are predominantly ~400-m- to 3-km-thick gradational zones. K-feldspar is compositionally distinct in eHD and neighboring gradational zones and shows no evidence of mixing. K-feldspar in a gradational zone between pHD and CP shows evidence of mixing between the two. Plagioclase in eHD and CP display distinct ranges of anorthite content, Sr, and light rare earth element abundances; both populations are observed in pHD. Major oxide and trace element calculations of melts in equilibrium with plagioclase cores indicate that the melts were more silicic, less calcic, and lower in Sr and Rb than corresponding analyzed whole-rock samples. These results suggest that the magmas also underwent plagioclase and biotite accumulation. The presence of two plagioclase populations in pHD is consistent with eHD and CP hybridizing to form pHD in an increasingly maturing and exchanging TIC magmatic system during the eHD-pHD-CP stages but before groundmass and small K-feldspar phenocrysts crystallized.

Louis Oppenheim https://orcid.org/0000-0001-5233-625X

INTRODUCTION

The concept that plutons are incrementally grown and can crystallize over several millions of years is widely accepted (e.g., Miller and Paterson, 2001; Coleman et al., 2004; Glazner et al., 2004; Matzel et al., 2006; Lipman, 2007; Schaltegger et al., 2009; Memeti et al., 2010, 2014; Schoene et al., 2012; Coint et al., 2013b; Samperton et al., 2015; Paterson et al., 2016). However, the physical and chemical characteristics of the magma batches that make up plutons and the degree to which they interact at the emplacement level to potentially form large magma mush bodies are extensively debated (e.g., Bartley et al., 2008; Memeti et al., 2010, 2014; Coleman et al., 2012; Barnes et al., 2016b; Paterson et al., 2016).

While field observations and whole-rock geochemical compositions have been widely utilized in the study of plutons, the "averaged" nature of these analyses at best restricts the ability to distinguish individual physical bodies and characterize detailed chemical processes that define arc magmas (e.g., mixing, recycling of mushes, fractional crystallization). Accessory minerals, such as zircon, and melt inclusions from volcanic and plutonic rocks have long been interpreted to indicate mixing and recycling of magmas based on patterns of age distribution and zircon composition (e.g., Bachmann and Bergantz, 2006; Matzel et al., 2006; Miller et al., 2007; Memeti et al., 2010; Siégel et al., 2018; Ratschbacher et al., 2018; Esposito et al., 2018). In other studies, distinct populations of minerals were identified based on textural and geochemical evidence and used to identify distinct magma pulses and possible mixing between pulses (Ginibre et al., 2002; Davidson et al., 2007; Zhang et al., 2015; Barnes et al., 2016b). Using mineral-scale compositions of rock-forming minerals in plutons is a relatively new approach to determining magma processes compared to similar studies of phenocrysts in volcanic rocks, but studies like those by Coint et al. (2013a), Barnes et al. (2016a, 2016b, 2019), and Werts et al. (2020) have demonstrated the utility of the method in identifying signatures of individual magma bodies, interconnectivity between magmas, and magma processes active during a pluton's history. Thus, magmatic histories are clearly preserved (cf. Challener and Glazner, 2017), even though plutonic magmas spend long periods cooling below the solidus.

MOTIVATION FOR STUDY

Incremental Emplacement and Resulting Magma Bodies in the Tuolumne Intrusion

The Tuolumne intrusive complex (TIC; California, USA) is a plutonic complex that has been widely studied to evaluate magma emplacement processes and petrology. By inference, the size of its active magma body (or bodies) during its 10 m.y. of hypersolidus activity is of great interest. Bateman and Chappell (1979) proposed that the TIC was emplaced as a single, large batch of magma that achieved compositional zoning through stepwise fractional crystallization and simultaneous upwelling of a hot, buoyant diapir tail, replenishing the large magma chamber. Kistler et al. (1986) subsequently showed that closed-system fractional crystallization could not have produced the Sr and Nd isotopic signatures found in each unit, implying that magma mixing of mantle- and crust-derived magmas in varying proportions was involved in forming the different TIC units (see also Gray et al., 2008). Thermal modeling studies raised the issue that a single magma pulse could not have remained above the solidus for the 10 m.y. lifespan of the TIC (e.g., Annen, 2009; Paterson et al., 2011; Gelman et al., 2013), and that multiple magma batches intruding at different times to revitalize the magma chamber(s) were required (Paterson and Vernon, 1995; Miller and Paterson, 1999; Coleman et al., 2004; Glazner et al., 2004; Memeti et al., 2010; Paterson et al., 2011).

Recent studies have focused on using the TIC, as well as other plutons, to investigate the nature of incremental growth of plutonic complexes and the degree of magma interconnectivity and hybridization between plutonic units at the emplacement level (e.g., McNulty et al., 2000; Glazner et al., 2004; Matzel et al., 2006; Miller et al., 2011; Coleman et al., 2012; Memeti et al., 2014; Paterson et al., 2016). One model (Coleman et al., 2004, 2012; Bartley et al., 2008, 2018) suggested that the main TIC units were emplaced as multiple sills or sheets, which interacted minimally (or not at all) with one another at the emplacement level and were subsequently folded. Coleman et al. (2012) described "cyclical," roughly north-south–striking compositionally distinct intrusive bodies ranging from granodiorite to leucogranite within the equigranular Half Dome Granodiorite in the southwestern portion of the TIC as evidence for the model. The "cycles" are interpreted to be the result of fractional crystallization of <1-km-thick intrusive sheets. This model argues that most compositional heterogeneity across the TIC was produced in the magma source region (Coleman et al., 2012).

An alternative model proposed that the interior TIC units amalgamated into an increasingly more extensive "magma mush body," beginning with the intrusion of the equigranular Half Dome magma (Žák and Paterson, 2005; Memeti et al., 2010, 2014; Paterson et al., 2016). This model is supported by a variety of outcrop-scale features. For example, gradational contacts are common between units at local and regional scales (Bateman and Chappell, 1979). These gradational zones are commonly interpreted as the result of either gradual fractional crystallization at the emplacement level (Economos et al., 2009; Memeti et al., 2010) or magmatic erosion and associated mineral and melt mixing at the "mushy" interface between units (Memeti et al., 2014; Barnes et al., 2016b; Paterson et al., 2016; Chambers et al., 2020). Materials interpreted to have been recycled from older units into younger ones include mixing features such as biotite clots in the Cathedral Peak unit that are interpreted to be pseudomorphs of Half Dome hornblende, and stoped blocks of older units in younger ones (Paterson, 2009; Paterson et al., 2016). Transitional zones are also present at interfaces between major units. They are composed of mineral populations that are characteristic of adjacent units (e.g., equigranular Half Dome hornblende and biotite books in a Kuna Crest transition, etc.) as determined by field characteristics and significant differences in trace element concentrations, as, e.g., in hornblende (Barnes et al., 2016b), which is also supported by whole-rock isotope compositions (Memeti et al., 2014). If mixing of individual units that are compositionally distinct from one another was ubiquitous across any two adjacent plutonic units of the TIC, it implies that magma hybridization of adjacent magmatic mushes occurred and could have formed extended mush zones. If so, similar evidence should be present in major and trace element signatures of other rock-forming minerals, such as plagioclase and K-feldspar.

Unraveling Magma Histories with Plagioclase and K-Feldspar

This study focuses on the characterization of K-feldspar and plagioclase crystal habits, compositions, and zoning patterns in the TIC using petrography, cathodoluminescence, and major and trace element analysis to identify potential feldspar recycling between individual TIC units to identify potential feldspar recycling between individual TIC units (see Supplemental File 1[1]). Feldspars were chosen because they are abundant and record different magmatic crystallization stages: plagioclase is a liquidus or near-liquidus phase, whereas K-feldspar crystallizes at lower hypersolidus temperatures. Thus, the two phases preserve an extensive magma crystallization record for the evolution of the TIC. Trace element zoning (both simple and oscillatory) is especially well preserved in the feldspars because they commonly incorporate slow-diffusing trace elements, such as Ba in K-feldspar (Moore and Sisson, 2008; Memeti et al., 2014) and Sr in both phases (Cherniak, 2002, 2010). K-feldspar in all units displays features that are distinguishable at outcrop and petrographic scales, such as mafic mineral inclusions oriented parallel to and within mineral growth zones. Although K-feldspar, in part, takes the form of megacrysts in the TIC interior, with lengths of as much as 15 cm (Bateman and Chappell, 1979; Memeti et al., 2014), minerals of this size will be discussed in a separate study. Rather, this study focuses only on three other K-feldspar morphologies: groundmass, smaller K-feldspar (~1 cm) phenocrysts, and medium-sized K-feldspar (4–6 cm) phenocrysts.

GEOLOGIC BACKGROUND

The TIC is a metaluminous, magnetite-series, composite intrusion comprising four major units that grade to more felsic and younger from the margins

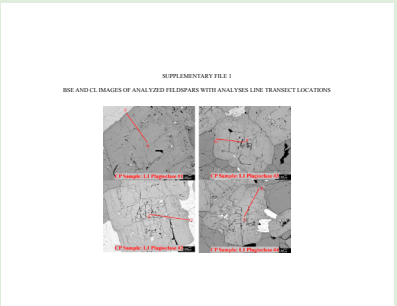
SUPPLEMENTARY FILE 1

BSE AND CL IMAGES OF ANALYZED FELDSPARS WITH ANALYSES LINE TRANSECT LOCATIONS

[1]Supplemental Material. Consists of BSE and CL images showing zonation in analyzed feldspar grains, EMPA analytical conditions, sample locations, and both whole rock and feldspar chemical data. Please visit https://doi.org/10.1130/GEOS.S.13228862 to access the supplemental material, and contact editing@geosociety.org with any questions.

to the interior. These units are, from margins to interior, the granodiorite of Kuna Crest and equivalent rocks, the Half Dome Granodiorite, the Cathedral Peak Granodiorite, and the Johnson Granite Porphyry (Bateman and Chappell, 1979; Kistler et al., 1986; Huber et al., 1989; Memeti et al., 2010, 2014) (Fig. 1).

The most extensive exposures of the granodiorite of Kuna Crest (KC) are in the KC lobe of the southeastern TIC. Equivalent tonalites and granodiorites crop out along the southern and western margins of the complex (Bateman and Chappell, 1979). U-Pb (zircon) ages range from 95 to 93 Ma (Kistler and Fleck, 1994; Coleman et al., 2004; Memeti et al., 2010, 2014; Paterson et al., 2016). The Half Dome Granodiorite ranges in age from 92 to 88 Ma (Kistler and Fleck, 1994; Coleman et al., 2004; Matzel et al., 2006; Memeti et al., 2010, 2014; Paterson et al., 2016) and is divided into two subunits: the older (92–90 Ma), outer, equigranular Half Dome Granodiorite (eHD), and the younger (90–88 Ma), inner, porphyritic Half Dome Granodiorite (pHD). The Cathedral Peak Granodiorite (CP) crystallized from 88 to 85 Ma (Kistler and Fleck, 1994; Coleman et al., 2004; Matzel et al., 2006; Memeti et al., 2010, 2014). The Half Dome and Cathedral Peak units, the focus of this study, are described in detail below.

In the southeastern TIC, both sharp and gradational interunit contacts are present (Žák and Paterson, 2005). In this area, all major TIC units are exposed in the transition from KC to the main body of the intrusion. It is this area that is the focus of this study (Fig. 1).

LITHOLOGIES, CONTACTS, AND FIELD RELATIONSHIPS OF THE SOUTHEASTERN TUOLUMNE INTRUSION

Figure 1 is a detailed map of the transition from the KC lobe to the main TIC body in the southeastern part of the complex. Mapping was conducted

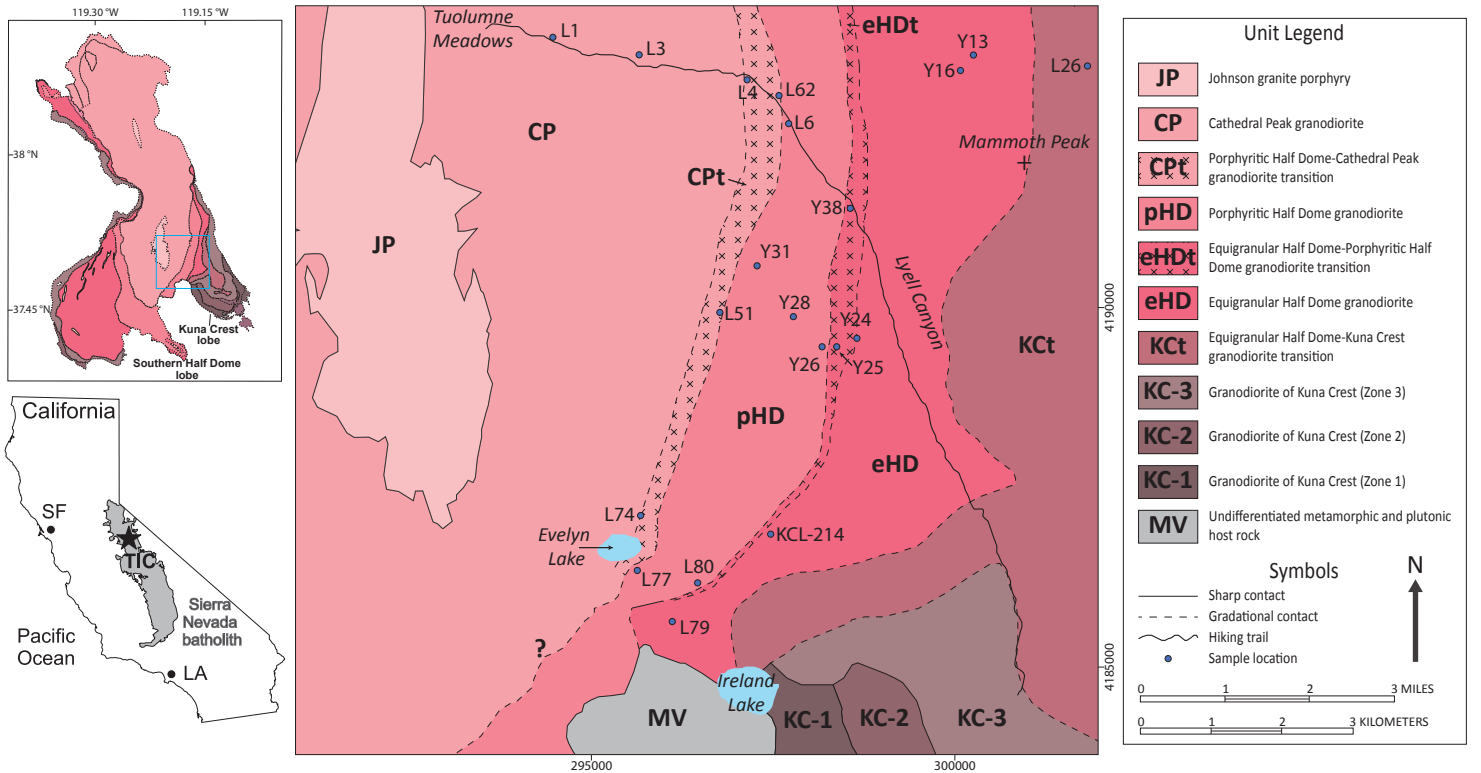

Figure 1. Geologic map of the field area in the granodiorite of Kuna Crest (KC) lobe transition to the main Tuolumne intrusive complex (TIC) intrusion (blue square in top inset map), including all major TIC units, transitional interunit contacts, and sample locations for this study (blue dots) (partially adapted from Bateman et al., 1983). The top inset map is the location of this study's field area within the TIC (adapted from Memeti et al., 2014). The bottom inset map is the location of the TIC within the Sierra Nevada batholith and the state of California (USA) (SF—San Francisco; LA—Los Angeles). Coordinates shown are in Universal Transverse Mercator in meters, zone 11N, with the North American Datum of 1927 (CONUS).

along three broad transects in this region: (1) Lyell Canyon; (2) Mammoth Peak; and (3) Evelyn Lake. Here, we describe all major TIC units exposed at the transition from the KC lobe to the main TIC body and the broad transitional contacts between each unit.

Kuna Crest and Transitional Kuna Crest Granodiorites

The KC in the southeastern lobe varies in composition from gabbro to tonalite to granodiorite (Bateman and Chappell, 1979; Memeti et al., 2014; Barnes et al., 2016b). Near the contact with the eHD, the KC is a medium-grained granodiorite characterized by subhedral hornblende, biotite, and gold-brown, euhedral to subhedral 1–5 mm titanite (Barnes et al., 2016b). The contact between KC and eHD is a transitional zone (KCt) (Fig. 2A) containing anhedral and subhedral hornblende, as well as euhedral biotite crystals larger than typical KC biotite and which resemble the habit and size of eHD biotite. Mafic minerals are typically lower in abundance in KCt than in KC and commonly form clots along with subhedral titanite. K-feldspar is subhedral and ~1 mm on its long axis, yielding a texture comparable to that of eHD. Plagioclase within this unit is white, euhedral, and blocky, ranging from 1 to 3 mm in length and displaying albite twinning. Quartz is anhedral, medium gray, translucent, and ≤1 mm in diameter. Accessory minerals such as zircon, apatite, titanite, and Fe-Ti oxides are also present but too small to be observed in hand sample. This ~3-km-wide transitional zone is in contact with a ~10-m-wide and 20–30-m-long mafic mineral–rich meladiorite zone at Mammoth Peak composed of euhedral and subhedral hornblende and biotite with minor plagioclase and accessory titanite.

Equigranular Half Dome and Transitional Equigranular Half Dome Granodiorites

The easternmost exposure of eHD analyzed is located at Mammoth Peak (Fig. 1). The eHD within much of the field area is characterized by 1–2-cm-long euhedral hornblende, ~1-cm-diameter euhedral biotite books, and euhedral titanite as long as 1 mm (Fig. 2B). Biotite and hornblende are of roughly equal modal abundance. K-feldspar, plagioclase, and quartz are approximately the same size and shape as in KCt.

The eHD-pHD contact is gradational across as much as 100 m in Lyell Canyon and much of the Evelyn Lake region, laterally thinning in the southern portion of the mapping area (Fig. 1). The contact approximately halfway between samples L77 and L79 is sharp (Fig. 1) and bounded on the pHD side of the contact by schlieren layers (layers of biotite, hornblende, plagioclase, and accessory minerals) and on both sides by swarms of microgranitoid enclaves. The sharp contact strikes roughly east-west and is steeply dipping at 83° (Fig. 2D).

Within the eHD-pHD transitional zone (eHDt; Fig. 2C), K-feldspar size and habit changes relative to that of eHD. While anhedral and <1 mm subhedral K-feldspar grains characteristic of the eHD are present in low abundances, most K-feldspars are euhedral, range from 1 to 2 cm in length, and contain more abundant, crystallographically aligned mafic mineral inclusions than eHD K-feldspar. Biotite and hornblende within this contact zone are euhedral and in lower modal abundances compared to eHD. Plagioclase and quartz in eHD and eHDt are generally the same size and shape, although rare plagioclase grains as long as 2 cm and quartz aggregates as much as 1 cm in diameter are present in eHDt.

Porphyritic Half Dome, Transitional Cathedral Peak, and Cathedral Peak Granodiorites

Like eHD, pHD is uniform in outcrop appearance, containing ~1-cm-diameter euhedral biotite books, subhedral to euhedral hornblende up to 1 cm long, and up to 1-cm-long euhedral titanite in places. Plagioclase and quartz are similar in size and shape to what is seen in eHD. The pHD unit is characterized by K-feldspar phenocrysts as long as 4 cm, which contain distinct, crystallographically aligned mafic mineral inclusions (Fig. 2E).

The contact between pHD and CP is gradational (referred to as CPt) with a maximum width of ~650 m in Lyell Canyon. The transition is characterized by clusters of K-feldspar megacrysts as long as 12 cm with relatively little matrix separating them (Figs. 2F, 2G). Smaller, 4–6-cm-long K-feldspar phenocrysts are also abundant in CPt. The cores of many of these 4–6-cm-long K-feldspar phenocrysts contain abundant, crystallographically aligned mafic mineral inclusions, whereas the outer zones of these crystals are relatively inclusion-poor (Fig. 2F). Similar inclusion patterns are observed in pHD K-feldspar phenocrysts. The CPt groundmass also contains K-feldspar ranging from 1 mm to 1 cm in size (Fig. 2h; these grains compose as much as 50% of the matrix near Evelyn Lake), both euhedral biotite books and anhedral biotite, and subhedral hornblende ranging to 1 cm long. Biotite is more abundant than hornblende within this gradational contact.

While plagioclase in CP is identical to CPt plagioclase in size and shape, CP contrasts significantly with CPt in terms of mafic mineral characteristics. Large euhedral hornblende and biotite that characterize eHD and pHD are absent in CP (although rare biotite clots in the shape of euhedral hornblende are present in some CP locations). Biotite in CP is typically anhedral and ~1 mm in diameter. The estimated modal abundance of mafic minerals in CP is lower than in pHD and eHD. The CP K-feldspar is also distinct from that of CPt. Most CP phenocrysts of the same size as those found in CPt and pHD lack mafic mineral inclusions and instead contain mostly plagioclase inclusions. The average size of K-feldspar phenocrysts is 3–5 cm in CP, with the size generally decreasing with distance from the CPt contact. Large quartz aggregates (as much as 2 cm across) are also common in CP.

ANALYTICAL AND IMAGING METHODS

Cathodoluminescence (CL) imaging of complete standard-sized thin sections was conducted at California State University (CSU) Fullerton using a CITL

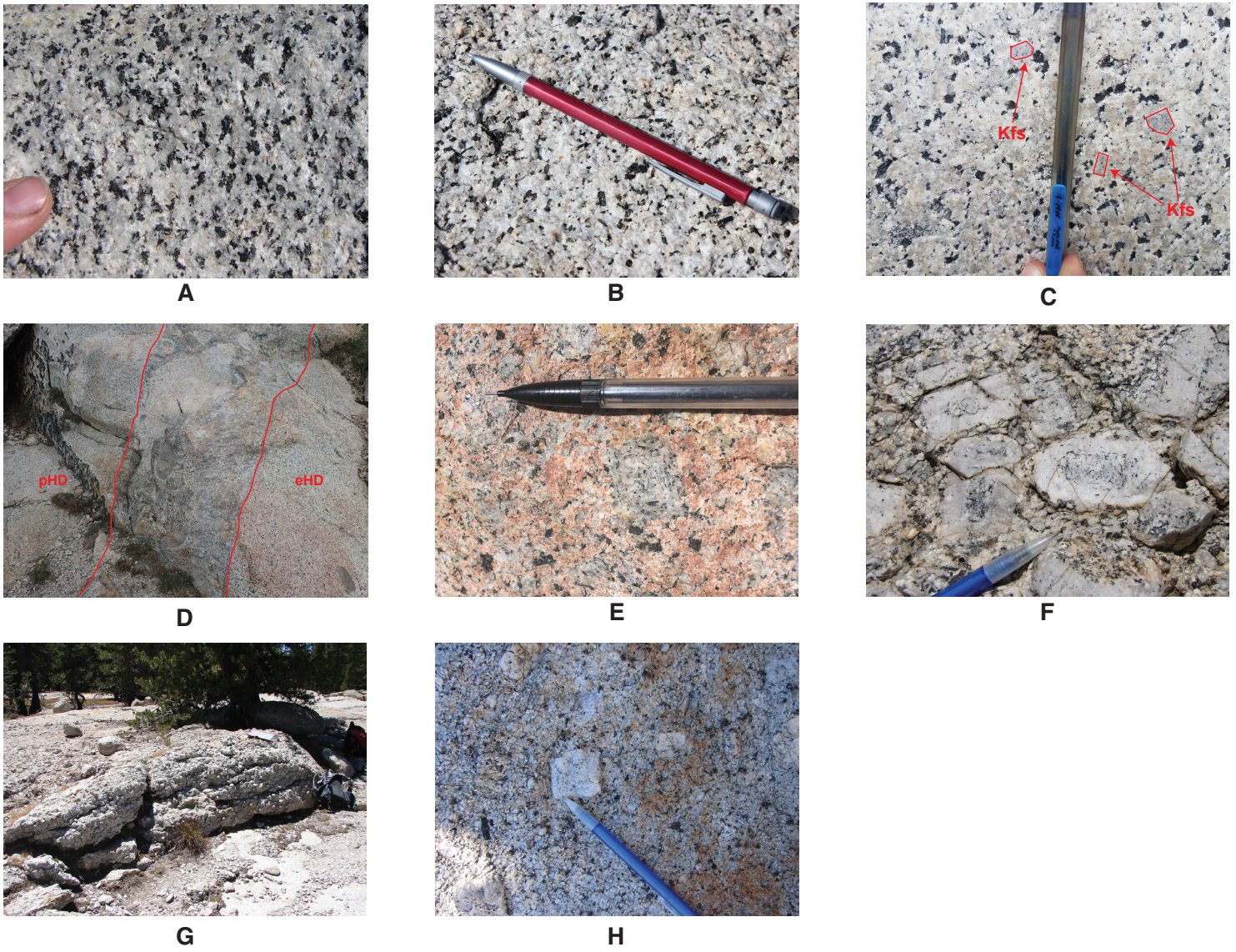

Figure 2. Photos of Tuolumne intrusive complex outcrops from Mammoth Peak and Lyell Canyon. (A) Transitional zone (KCt) between granodiorite of Kuna Crest (KC) and equigranular Half Dome Granodiorite (eHD). (B) Unit eHD. (C) Transitional zone (eHDt) between eHD and porphyritic Half Dome Granodiorite (pHD) with increased (relative to eHD) abundance in quartz and larger K-feldspar (Kfs) phenocryst size (grains outlined in red). (D) Sharp contact at Evelyn Lake between eHD and pHD, marked with a ~1-m-wide mingling zone on the pHD side. (E) Unit pHD with mafic inclusion–rich K-feldspar phenocrysts as large as 4 cm. (F) Transitional zone (CPt) between pHD and Cathedral Peak Granodiorite (CP) with K-feldspar megacrysts as long as 12 cm (some of which have mafic mineral inclusion–rich cores). (G) Outcrop view of K-feldspar megacryst-rich sheets in CPt. (H) Unit CP granodiorite and granite with inclusion-poor K-feldspar phenocrysts as large as 7 cm.

CL8200 Mk5-2 cathodoluminescence attachment set at 10 kV and mounted on a Nikon SMZ18 stereoscope. Thirty (30) to 40 photomicrographs of parts of each thin section were taken at high magnification using a Nikon DS-Fi2 camera attached to the stereoscope and stitched together to show the luminescence across the full thin section using Nikon NIS-Elements software.

Whole-rock X-ray fluorescence (XRF) analysis was conducted on glass beads fused from rock powders (pulverized in a Shatterbox tungsten-carbide vessel) and Spectromelt A10 (di-lithium tetraborate) flux using a 1:2 ratio at CSU Fullerton, generally following procedures of Johnson et al. (1999). These beads were analyzed using a 3.0 kW Panalytical Axios wavelength-dispersive XRF spectrometer at Pomona College (Claremont, California). Each analysis represents an average of three measurements.

Electron microprobe analysis (EMPA) of K-feldspar and plagioclase was conducted at University of California, Los Angeles, using a JEOL JXA-8200 Superprobe equipped with five wavelength-dispersive X-ray spectrometers. Additional EMPA analyses of plagioclase and K-feldspar in samples KCL-214 and KCL-536 (not shown in Fig. 1) were done with a JEOL JXA-8200 Superprobe at the Max-Planck Institute for Chemistry (Mainz, Germany). We analyzed SiO_2, Al_2O_3, CaO, Na_2O, K_2O, FeO, MgO, MnO, TiO_2, and Cr_2O_3 (see Supplemental File 2 [footnote 1] for EMPA analytical conditions).

Trace element concentrations in K-feldspar and plagioclase were determined using laser ablation–inductively coupled plasma–mass spectrometry (LA-ICP-MS). Analyses were conducted at Texas Tech University using a New Wave UP213 Nd-YAG laser ablation system attached to an Agilent 7500cs inductively coupled quadrupole plasma mass spectrometer. Laser conditions were nominal 5% energy, a repetition rate of 5 Hz, and a fluence range of 1.31–1.95 mJ. Ablation spots were 60 µm in diameter and were placed over EMPA analysis spots. Trace element isotopes analyzed were ^{7}Li, ^{27}Al, ^{29}Si, ^{31}P, ^{43}Ca, ^{47}Ti, ^{57}Fe, ^{66}Zn, ^{69}Ga, ^{85}Rb, ^{88}Sr, ^{89}Y, ^{90}Zr, ^{133}Cs, ^{137}Ba, ^{139}La, ^{140}Ce, ^{141}Pr, ^{146}Nd, ^{147}Sm, ^{153}Eu, ^{157}Gd, ^{159}Tb, ^{163}Dy, ^{165}Ho, ^{166}Er, ^{169}Tm, ^{172}Yb, ^{175}Lu, and ^{208}Pb. EMPA-determined CaO and SiO_2 were used as internal standards for data reduction in plagioclase and K-feldspar analyses, respectively. U.S. Geological Survey (USGS) glass GSD was used as the calibration reference material and to control for instrument drift. USGS glass BHVO-2G was used to monitor precision and accuracy. Uncertainties for each trace element were determined based on the relative standard deviation of glass BHVO-2G measurements acquired throughout each day of analysis.

Additional LA-ICP-MS analyses of K-feldspar and plagioclase in samples KCL-214 and KCL-536 were conducted using a New Wave UP193 Nd-YAG laser ablation system coupled to a Thermo Finnigan Element2 double-focusing sector field ICP-MS at the Max-Planck Institute for Chemistry. Spots of 60 µm diameter were ablated with the laser at a fluence of ~4 J/cm^2 and a repetition rate of 10 Hz. The ICP-MS was used in the low-resolution mode. The gas blank was measured prior to the ablation of the sample for 15 s followed by a dwell time of 70 s on the sample and a wash time of 60 s. Trace element isotopes analyzed were ^{7}Li, ^{29}Si, ^{43}Ca, ^{49}Ti, ^{61}Ni, ^{62}Ni, ^{85}Rb, ^{88}Sr, ^{89}Y, ^{90}Zr, ^{93}Nb, ^{133}Cs, ^{137}Ba, ^{139}La, ^{140}Ce, ^{141}Pr, ^{146}Nd, ^{147}Sm, ^{151}Eu, ^{157}Gd, ^{159}Tb, ^{163}Dy, ^{165}Ho, ^{167}Er, ^{169}Tm, ^{173}Yb, ^{175}Lu, ^{178}Hf, ^{181}Ta, ^{208}Pb, ^{232}Th, and ^{238}U. U.S. National Institute of Standards and Technology (NIST) glass standard 612 was used for tuning of the mass spectrometer first for maximum intensity on La and Th and then for low oxide rate (Th/ThO_2 <0.3%). The same reference material was also analyzed for the determination and monitoring of the drift of the relative sensitivity. Trace element concentrations were calculated using a Microsoft Excel spreadsheet. The analytical procedure is described in detail by Jochum et al. (2006, 2007).

Element concentrations in line plots are shown with rim compositions at the origin due to the fact that the grains have significant variability in grain size. Additionally, it is difficult to determine when the different sized populations and/or their cores commenced growth, but it is likely that their rims all ceased growth at the time of final melt crystallization, especially where in contact with a low-temperature magmatic phase. Feldspar populations are determined based on petrographic and geochemical characteristics. Individual feldspars are determined geochemically as the same population if they (1) share similar core-to-rim element variations and (2) are along a similar fractionation array as defined by two elements.

WHOLE-ROCK COMPOSITONAL PATTERNS ACROSS TUOLUMNE INTRUSIVE COMPLEX UNITS

Seventeen (17) rock samples were collected along the three broad transects in Lyell Canyon, at Mammoth Peak, and near Evelyn Lake (Fig. 1; Supplemental File 3 [footnote 1]). Also included are samples KCL-536 (KCt) and KCL-214 (eHD) from Barnes et al. (2016b) (see Supplemental Files 4 and 5 for whole-rock major oxide and trace element compositions, respectively). The samples are classified as granite, granodiorite, and quartz monzonite on the plutonic rock classification of Middlemost (1994), with the majority of the samples plotting as granodiorite (Fig. 3). Silica contents in the major units (i.e., eHD, pHD, and CP) generally increase from the Kuna Crest margins toward the southeastern CP near Tuolumne Meadows. Transitional units vary in composition as follows (Fig. 3): SiO_2 contents are lower in two samples from KCt (samples L26A from Mammoth Peak [Fig. 1] and KCL-536 from the KC lobe [Barnes et al., 2016b]) than most eHD samples. Sample L79 (eHD; Fig. 1) is the exception, with approximately the same SiO_2 as the two KCt samples. In contrast, samples Y25 and Y38 (eHDt; Fig. 1) contain considerably more SiO_2 than is typical of eHD and pHD samples and are therefore classified as granite. CPt samples are the most heterogeneous of the transitional samples, with two samples plotting as quartz monzonite (similar to pHD) and one plotting at higher silica than CP and pHD.

Major oxide and trace element compositions reveal additional patterns when comparing units (Fig. 4; Supplemental File 6 [footnote 1]). TiO_2, P_2O_5, MgO, CaO, and FeO all decrease with increasing SiO_2, which is consistent with observations from other parts of the Tuolumne intrusion (Bateman and Chappell, 1979; Gray et al., 2008). As expected, the latter three oxides show the highest negative correlation with SiO_2, although two CPt samples plot below the generally negative linear FeO trend (Fig. 4A). Trace elements Sr, Ba, and

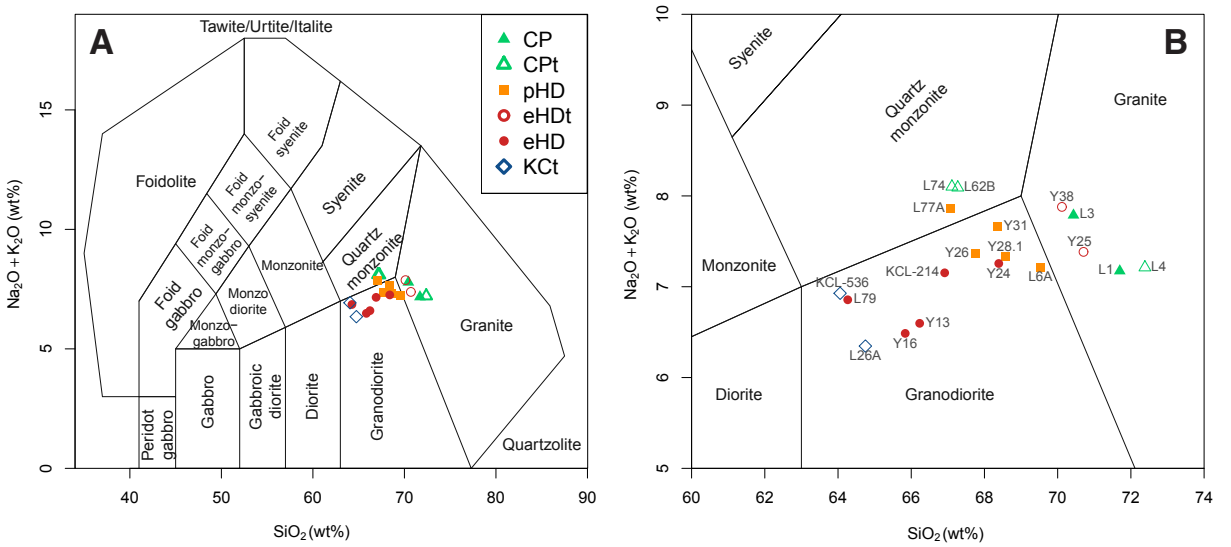

Figure 3. Middlemost (1994) rock classification of Tuolumne intrusive complex (TIC) whole-rock samples based on X-ray fluorescence data. Units are Cathedral Peak Granodiorite (CP), transitional Cathedral Peak Granodiorite (CPt), porphyritic Half Dome Granodiorite (pHD), transitional equigranular Half Dome Granodiorite (eHDt), equigranular Half Dome Granodiorite (eHD), and transitional Kuna Crest Granodiorite (KCt). (A) Classification plot including all whole-rock samples, color coded by unit. (B) Close-up view of the quartz monzonite–granite–granodiorite fields of A showing each whole-rock sample labeled with sample number for reference (see Fig. 1 for sample locations).

Y also generally decrease with increasing SiO_2. Compared to KCt, eHD, and most pHD samples, however, Ba is elevated in one pHD sample and the two least-silicic CPt samples (Fig. 4B). Two distinct groupings can be identified when whole-rock values of Sr are compared with SiO_2 (Fig. 4C): one group is defined by lower Sr concentrations and consists of samples from KCt, eHD, and eHDt; the other group contains higher Sr contents and consists of samples from pHD, CPt, and CP. Two similar groupings can also be identified in Y contents, with KCt and eHD containing Y >11 ppm and the remaining units plotting at <9 ppm (Fig. 4D). The patterns of eHDt in Y content is distinct from its patterns in Sr content, with eHDt overlapping in Y composition with pHD, CPt, and CP.

Comparison of data from southern Half Dome lobe samples from Economos et al. (2009) with data from this study shows that the southern Half Dome and pHD samples commonly overlap in chemical composition. The comparison is especially noticeable in Figure 4C, where most pHD samples plot at the same Sr contents as southern Half Dome lobe samples with similar SiO_2. Figures 4B and 4D similarly show that some pHD samples plot at the same Ba and Y and southern Half Dome samples with similar SiO_2. In contrast, KCt and eHD samples plot at lower Ba and Sr and higher Y than southern Half Dome samples.

PETROGRAPHIC CHARACTERISTICS OF K-FELDSPAR

Potassium feldspar from KCt and much of eHD (Fig. 5A) is typically subhedral to anhedral and ~1–5 mm in length. Mineral inclusions include plagioclase, apatite, biotite, and hornblende, and less commonly titanite and zircon. These inclusions average ~250 µm in length and are concentrated in the cores. They are not aligned parallel to any crystallographic orientation in the host grain, as is typical in the other TIC units (see below). Tartan-plaid twinning, characteristic of microcline, as well as microperthite and simple twinning are observed in some but not all K-feldspar in KCt and eHD.

Within eHDt, K-feldspar grains vary in habit, size, and abundance. K-feldspar is predominantly ~1 cm in length on average and exhibits a boxy, euhedral habit with a thin, outer anhedral rim, which is intergrown with the groundmass. Inclusions within these grains follow a crystallographically defined orientation. The minerals included in these grains are the same as those found in eHD, with the addition of quartz (Fig. 5B). Twinning is commonly tartan and/or simple twinning.

Potassium feldspar grains from pHD, CPt, and CP are similar in petrographic characteristics (Fig. 5C). Grains from all three units are euhedral with thin rims that fill interstices in the groundmass, contain abundant crystallographically oriented mineral inclusions, and are commonly simple and tartan twinned

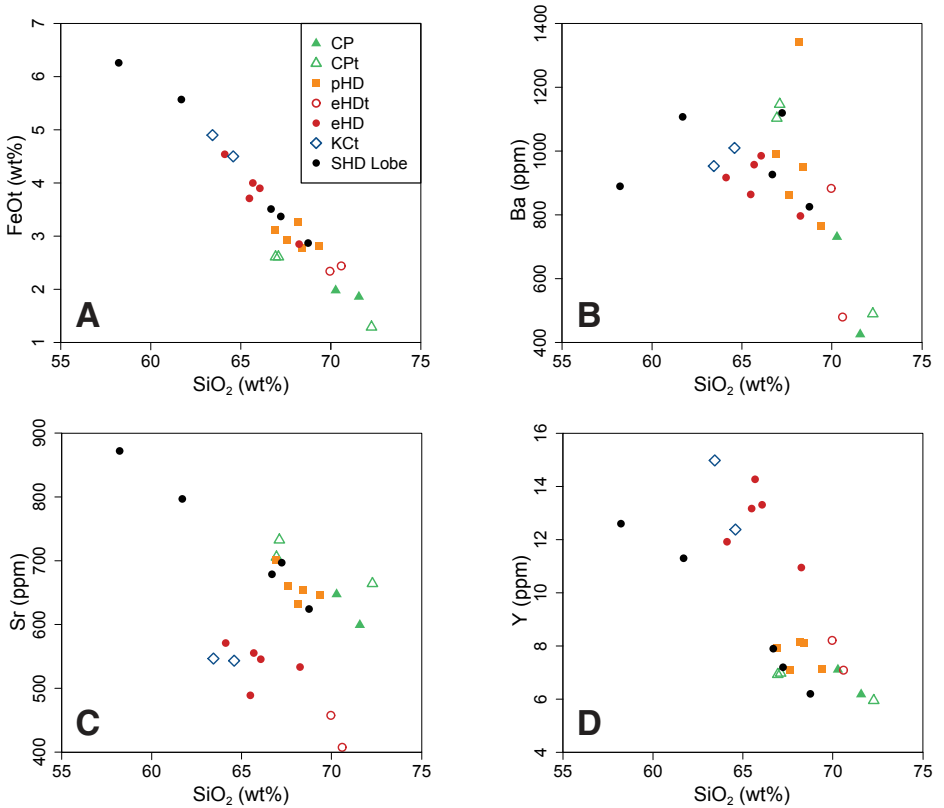

Figure 4. X-ray fluorescence whole-rock geochemistry. (A) FeO (wt%) versus SiO_2 (wt%). (B) Ba (ppm) versus SiO_2 (wt%). (C) Sr (ppm) versus SiO_2 (wt%). (D) Y (ppm) versus SiO_2 (wt%). Units are Cathedral Peak Granodiorite (CP), transitional Cathedral Peak Granodiorite (CPt), porphyritic Half Dome Granodiorite (pHD), transitional equigranular Half Dome Granodiorite (eHDt), equigranular Half Dome Granodiorite (eHD), transitional Kuna Crest Granodiorite (KCt), and southern Half Dome (SHD) lobe.

with abundant microperthite. From one unit to the next, K-feldspar grains are distinct in terms of relative abundances of mineral inclusions. K-feldspar phenocrysts from pHD and CPt commonly contain euhedral hornblende inclusions along with plagioclase, biotite, titanite, apatite, and zircon. In contrast, K-feldspar phenocrysts from CP contain abundant plagioclase inclusions and few inclusions of hornblende and biotite. In addition to phenocrysts, interstitial anhedral K-feldspar is present in all three units (Fig. 5D).

POTASSIUM FELDSPAR ZONING PATTERNS OBSERVED WITH CATHODOLUMINESCENCE

Cathodoluminescence images (Fig. 6) of K-feldspar exhibit dark blue to bright blue colors regardless of the unit to which they belong. Red patchy zones are observed in some grains. The change between dark and bright blue color in K-feldspar is attributed to the density of Al-O^--Al structural defects resulting from the coupled substitution of Ba^{2+} for K^+ and Al^{3+} for Si^{4+} (Viswanathan and Brandt, 1980; Viswanathan and Kielhorn, 1983; Słaby et al., 2008). This substitution maintains the charge balance when Ba^{2+} substitutes for K^+ and thus can be used as a rough proxy for Ba (and Al) content (Słaby et al., 2008). Słaby et al. (2008) noted a correlation between the density of crystal defects and mineral trace element compositions and related it to the degree of hybridization in the Karkonosze granite (Bohemian massif), showing the use of CL to be valuable in the study of magma mixing.

Cathodoluminescence zoning in K-feldspar typically differs between units, specifically by changes from dark to bright blue. KCt and eHD K-feldspar (Fig. 6A) exhibit simple, normal zoning in which subhedral grains have bright blue cores that grade into darker blue rims. The eHDt K-feldspar (Fig. 6B), in some cases, has a simple, normal zoning pattern, as in KCt and eHD, but the boundary between blue shades is sharp. This sharp boundary is also marked by round quartz inclusions in the innermost rim zone. In other cases, K-feldspar has bright blue outer rims (not shown in Fig. 6B). K-feldspar phenocrysts in

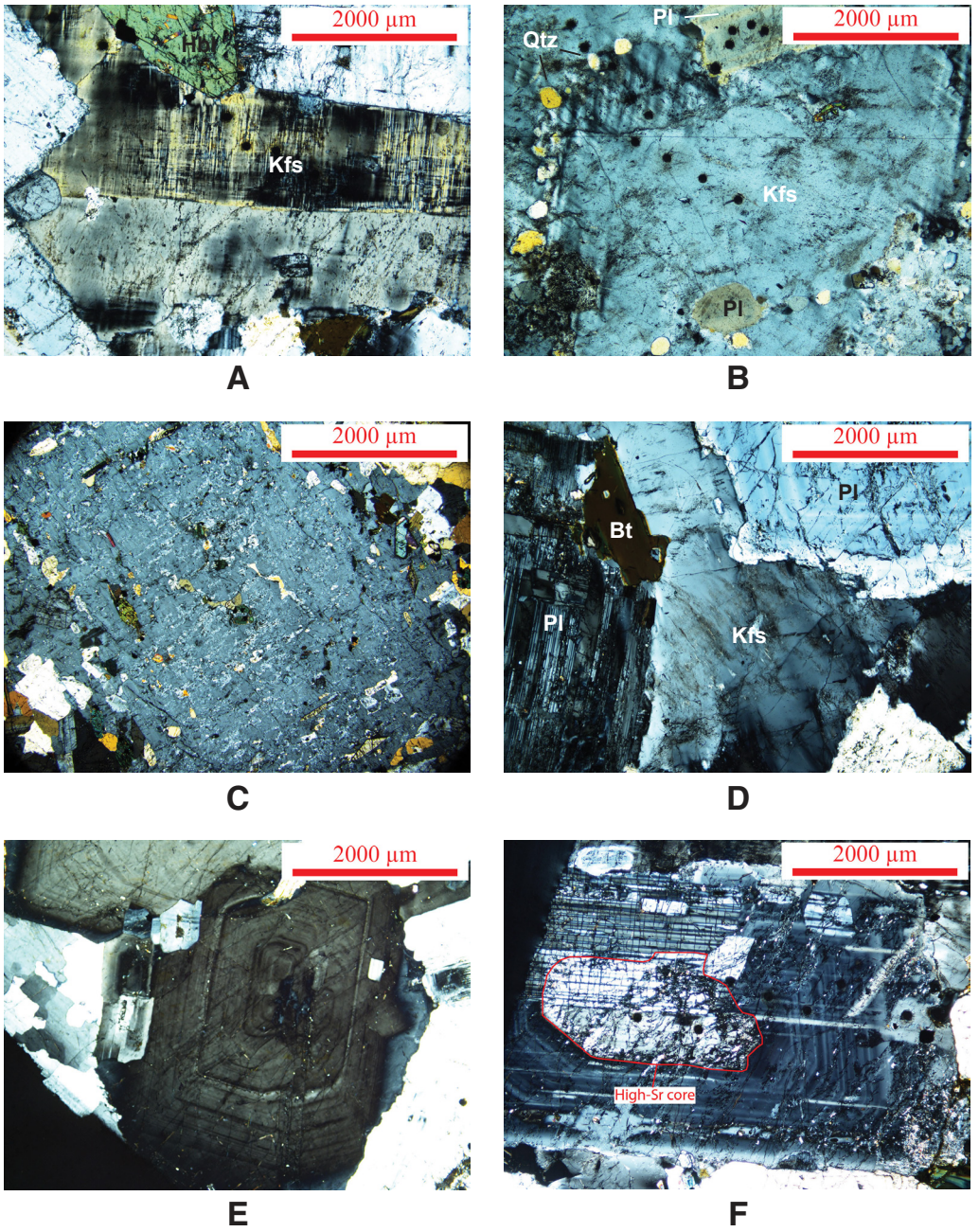

Figure 5. Photomicrographs of representative feldspar grains from Tuolumne intrusive complex (TIC) thin sections. Laser ablation spots (dark dots forming a line) are present in A, B, and F. (A) Subhedral K-feldspar from equigranular Half Dome Granodiorite (eHD) (from sample Y13) with gridiron and simple twinning (latter type of twinning in eHD is rare). (B) Euhedral K-feldspar from the transitional zone (eHDt) between eHD and porphyritic Half Dome Granodiorite (pHD) (from sample Y38) with a "ring" of circular quartz and euhedral plagioclase surrounding its core. (C) Euhedral K-feldspar phenocryst from pHD sample L77A with multiple zones of crystallographically oriented plagioclase, hornblende, and titanite inclusions. (D) Anhedral K-feldspar in pHD (from sample L77A) filling gaps between euhedral plagioclase and biotite (this type of K-feldspar is also observed in eHDt, pHD, Cathedral Peak Granodiorite [CP], and transitional zone [CPt] between pHD and CP). (E) Representative euhedral TIC plagioclase from CP sample L3 exhibiting oscillatory zoning. (F) CPt plagioclase (from sample L62A) with oscillatory zoning, with a resorbed core outlined in red. Minerals are abbreviated following the classification scheme of Kretz (1983): Qtz—quartz; Kfs—K-feldspar; Pl—plagioclase; Hbl—hornblende; Bt—biotite.

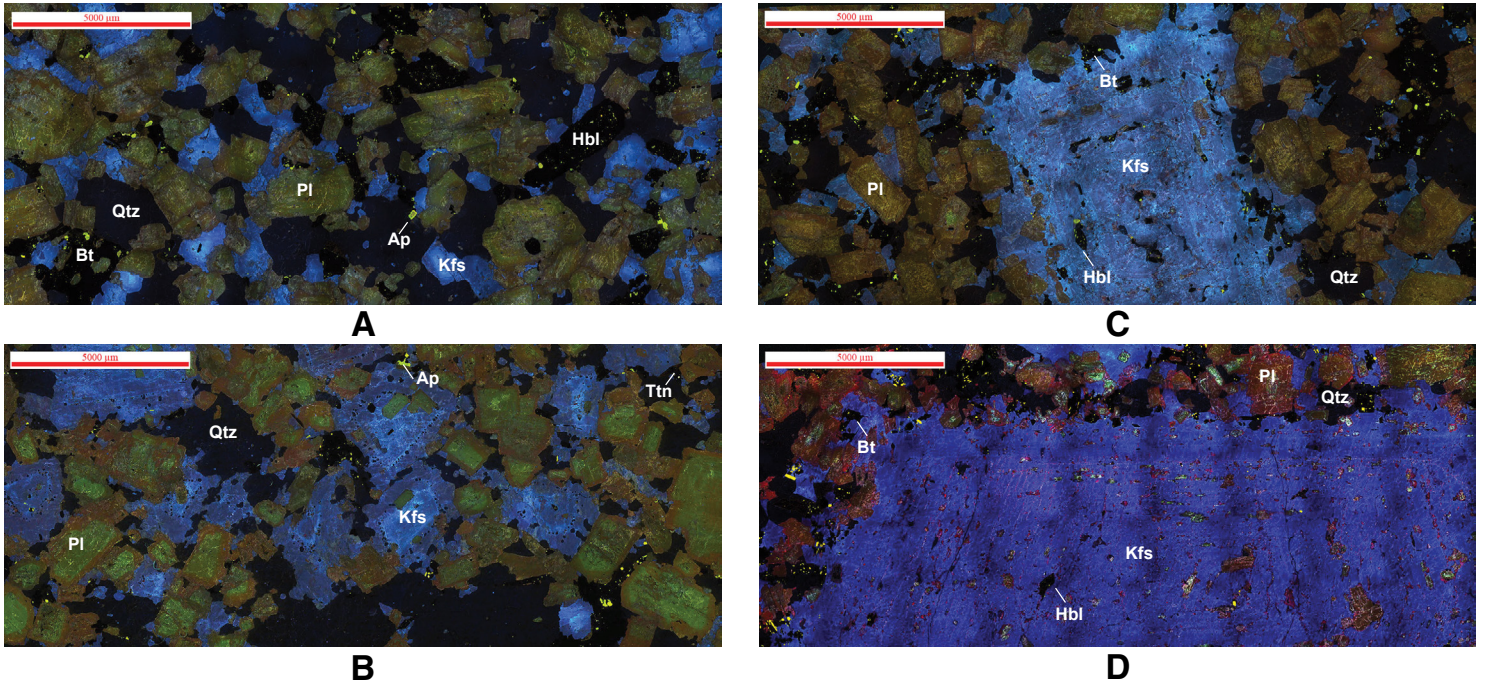

Figure 6. Photomicrographs of Tuolumne intrusive complex thin sections observed under cathodoluminescence (CL) with a stereoscope. (A) Equigranular Half Dome Granodiorite (eHD) sample L79. (B) Granite sample Y38 from the transitional zone (eHDt) between eHD and porphyritic Half Dome Granodiorite (pHD). (C) pHD granodiorite sample L77A. (D) Cathedral Peak Granodiorite (CP) sample L3B. Transitional units between granodiorite of Kuna Crest and eHD (KCt) and between pHD and CP (CPt) (not shown) are indistinguishable from eHD and CP, respectively. K-feldspar (Kfs), plagioclase (Pl), and apatite (Ap) under CL display blue, green to reddish-brown, and yellowish-green colors, respectively. Quartz (Qtz) faintly luminesces as navy blue. Hornblende (Hbl), biotite (Bt), and titanite (Ttn) do not luminesce under CL, thus appearing black. Dark regions within large grains are artifacts from "stitching" of separate images and are not related to grain behavior under CL. Mineral abbreviations follow the classification scheme of Kretz (1983).

pHD, CPt, and CP (Figs. 6C, 6D) are oscillatory zoned, where bright and dark blue zones alternate, but rims commonly luminesce dark blue. Bright blue zones display sharp inner contacts with the CL color of individual zones grading to darker shades of blue outward. The number of these oscillatory zones is similar between units because the phenocrysts analyzed in this study are roughly the same size (as large as 4 cm). Anhedral groundmass K-feldspars from eHDt, pHD, CPt, and CP are consistently dark blue, showing no zoning under CL.

PETROGRAPHIC CHARACTERISTICS OF PLAGIOCLASE

Plagioclase grains show few to no petrographic characteristics that are distinctive of individual units. Plagioclase is typically euhedral, varies from <1 mm to 1 cm in length, and commonly exhibits albite and/or simple twinning. Most grains have distinct oscillatory zoning under cross-polarized light (Fig. 5E), and the boundaries between zones vary from sharp to gradational. Mineral inclusions are uncommon but, where present, are typically near plagioclase rims. The most common inclusions are plagioclase, apatite, biotite, and hornblende, while zircon is rare. The cores of some eHD plagioclase grains contain abundant hornblende inclusions; these types of grains are rare. In CP, and less commonly pHD and CPt, plagioclase contains resorbed cores with distinct extinction angles and twinning relative to the surrounding rim (Fig. 5F). These more calcic cores are commonly resorbed and, in some cases, are altered to sericite.

PLAGIOCLASE ZONING PATTERNS OBSERVED WITH CATHODOLUMINESCENCE

Unlike K-feldspar, plagioclase has a relatively consistent zoning pattern from unit to unit (Fig. 6). Plagioclase cores and interiors (i.e., zones between

the cores and rims of grains) commonly exhibit a light- to medium-olive-green color throughout the grains, commonly with a sharp change to brown or red at their rims. Several grains have yellowish-brown cores as well, although they are not characteristic of a specific unit. Oscillations between shades of green and brown in plagioclase interiors are rare. Resorption textures observed in eHDt plagioclase in cross-polarized light are observed in CL as brown patches overprinting green to yellow cores and interiors. Distinct cores with sericite observed mostly in CP under cross-polarized light are present in CL as bright green colors relative to surrounding olive-green interiors (abundant in Fig. 6D). Marshall (1988) attributed the colors described in plagioclase to specific activators (or trace elements that luminesce in specific minerals). Green-to-yellow zones are attributed to Mn^{2+} and/or Fe^{2+} substitution, while red zones are attributed to Fe^{3+} substitution. As with K-feldspar, Al-O^{-}-Al is an important CL activator during coupled substitution in plagioclase, especially in magma-mixing environments (Słaby et al., 2008).

POTASSIUM FELDSPAR MAJOR AND TRACE ELEMENT COMPOSITIONS

Orthoclase Content

Analysis of orthoclase (Or) content in K-feldspar from the different TIC units yields indistinguishable Or content ranges (Table 1; Supplemental File 7 [footnote 1]). The maximum Or content for all units is 97 mol% (Or_{97}), and the minimum is Or_{85}. The values shown in Table 1 do not account for albite exsolution. One analyzed perthite domain from a pHD phenocryst in sample L77A was used to determine the grain's original Or content. Original Or content was calculated based on that of exsolution lamellae and a neighboring K-feldspar zone. Exsolution lamellae were approximated as composing 10% of a backscattered electron image by area, while K-feldspar was approximated as the remaining 90%. This calculation is depicted in the following equation (Kfs is K-feldspar):

$$(Or_{lamellae} \times 0.1) + (Or_{Kfs} \times 0.9) = Or_{KfsOriginal}. \quad (1)$$

The lamellae measured yield values of An_5-Ab_{90}-Or_5 (An is anorthite; Ab is albite). Correction for exsolution yields an original composition of Or_{86}, about the same value as the lowest Or content analyzed.

Trace Elements

In contrast to major elements (Supplemental File 8 [footnote 1]), several trace elements yield distinct results for K-feldspar from the different TIC units in both concentration and zoning pattern (Supplemental File 9). Figure 7 shows rim-to-core trace element profiles from representative K-feldspar grains from each unit, determined as representative by zoning pattern and trace element abundances. Besides eHDt, each unit is represented by one grain in Figures 7C–7L due to most grains within each unit overlapping in composition

TABLE 1. ORTHOCLASE (Or) CONTENT RANGE OF K-FELDSPAR (Kfs) AND ANORTHITE (An) CONTENT RANGE OF PLAGIOCLASE (Pl) FROM INDIVIDUAL TUOLUMNE INTRUSIVE COMPLEX (TIC) UNITS

TIC unit	Kfs Or content range	Plg An content range	No. of grains analyzed	Notes
KCt	Or_{94}–Or_{87}	An_{50}–An_{18}	Kfs: 8 Pl: 5	
eHD	Or_{96}–Or_{87}	An_{42}–An_{15}	Kfs: 16 Pl: 11	One plagioclase core at An_{86}
eHDt	Or_{97}–Or_{87}	An_{40}–An_{15}	Kfs: 7 Pl: 6	
pHD	Or_{96}–Or_{85}	An_{42}–An_{15}	Kfs: 9 Pl: 17	One plagioclase core at ~An_{45}
CPt	Or_{94}–Or_{86}	An_{33}–An_{14}	Kfs: 4 Pl: 9	An_{45}–An_{42} core in one plagioclase; two rims with <An_{10}
CP	Or_{95}–Or_{88}	An_{30}–An_{12}	Kfs: 2 Pl: 10	Multiple plagioclase cores with An_{33}–An_{43}; two rims with <An_{10}
SHD lobe margin	Or_{95}–Or_{88}	An_{30}–An_{12}	Kfs: 2 Pl: 3	
SHD lobe center	Or_{91}–Or_{89}	An_{30}–An_{12}	Kfs: 1 Pl: 3	One plagioclase core at An_{46}; one plagioclase rim at An_2

Note: SHD—southern Half Dome.

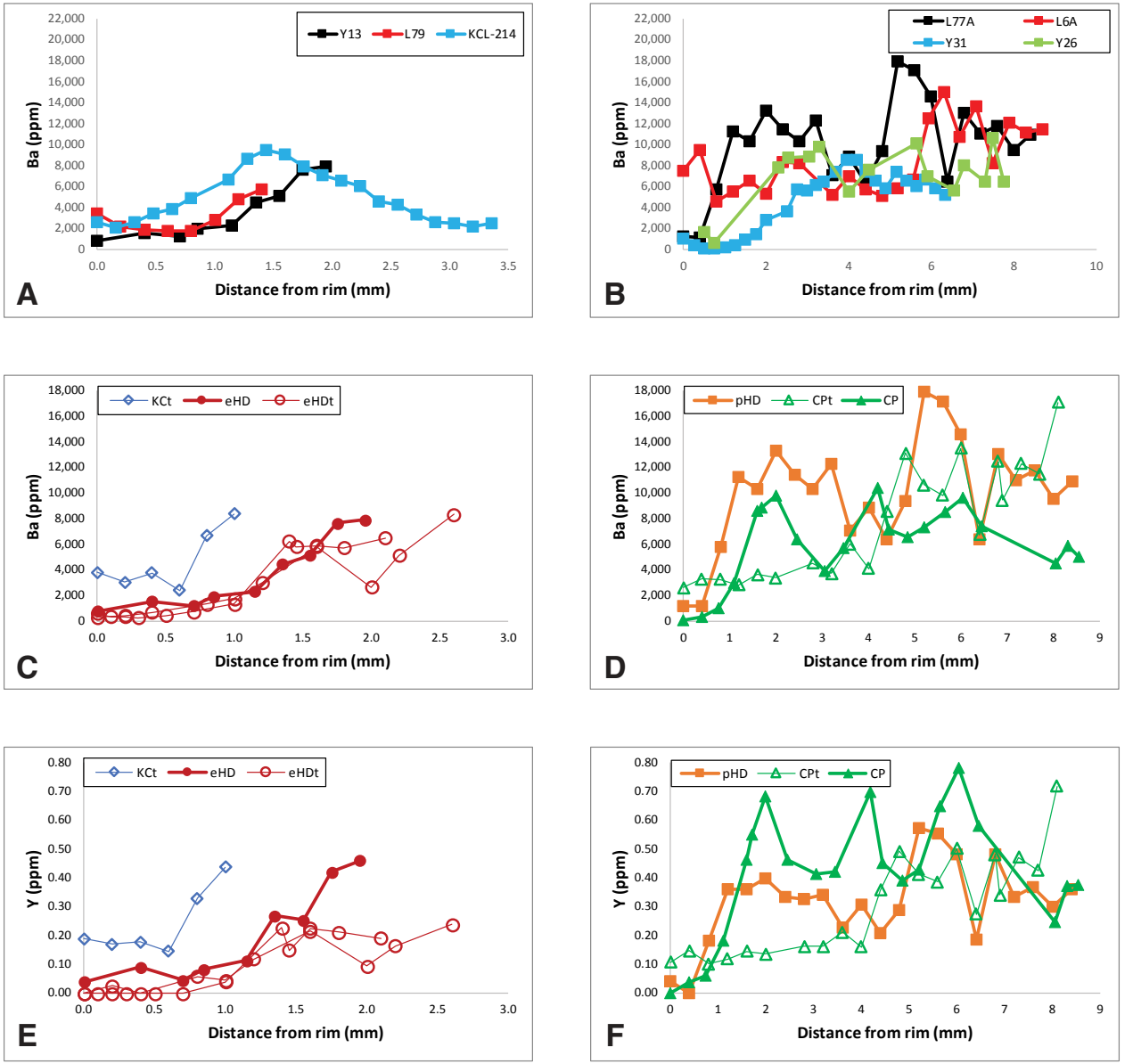

Figure 7. Profiles depicting trace element variations in representative Tuolumne intrusive complex K-feldspars, from rim (left) to core (right). Unit abbreviations: KCt—transitional zone between granodiorite of Kuna Crest (KC) and eHD; eHD—equigranular Half Dome Granodiorite; eHDt—transitional zone between eHD and pHD; pHD—porphyritic Half Dome Granodiorite; CPt—transitional zone between pHD and CP; CP—Cathedral Peak Granodiorite. (A) Comparison of Ba (ppm) in different K-feldspars from eHD samples (sample KCL-214 is a rim-to-rim traverse). (B) Comparison of Ba (ppm) in different K-feldspars from pHD samples. (C–L) Comparison of trace elements (ppm) in groundmass K-feldspar from KCt, eHD, and eHDt (C, E, G, I, and K), and in K-feldspar phenocrysts from pHD, CPt, and CP (D, F, H, J, and L). (C, D) Ba. (E, F) Y. (G, H) Sr. (I, J) Rb. (K, L) Ti. (*Continued on following page.*)

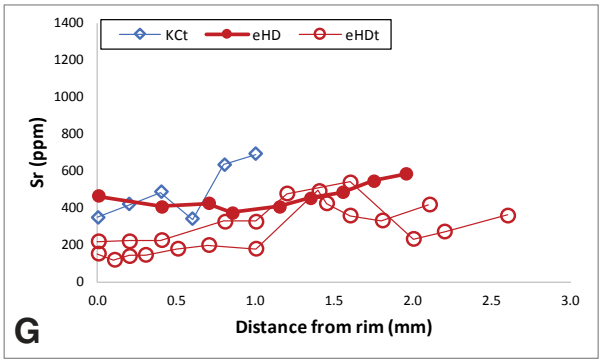

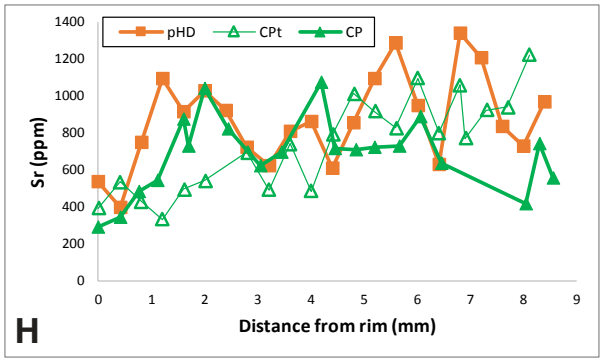

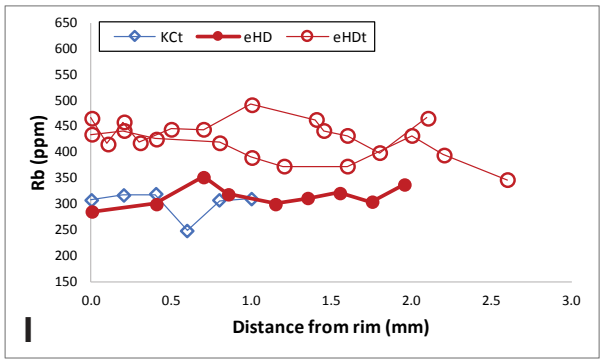

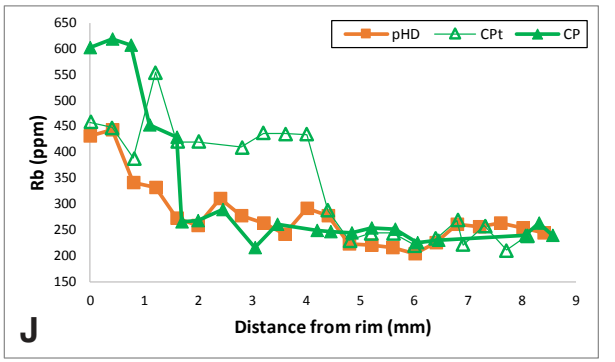

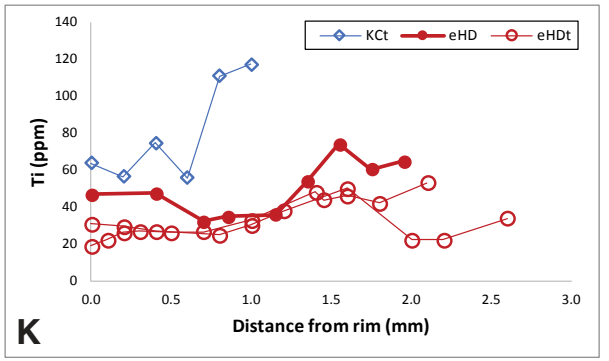

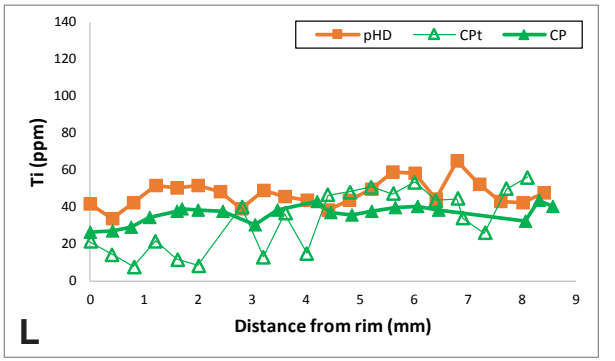

Figure 7 (*continued*).

(as demonstrated in Figs. 7A and 7B). The highly abundant trace element Ba (Figs. 7C, 7D) is variable in zoning pattern and abundance between units. Subhedral eHD and KCt K-feldspars exhibit a simple zoning pattern with a gradual decrease in Ba concentration from core to rim (Ba ranges from 800 ppm to 9500 ppm). Several K-feldspars in eHDt, like eHD K-feldspars, exhibit simple Ba zoning, although Ba concentration drops sharply from core to interior (~6500 ppm in the core to ≤1300 ppm in the interior and rim). Other K-feldspars from eHDt (more similar to eHD in hand-sample appearance) exhibit simple zoning with a dip and peak in the interiors (Ba ranges from 8000 ppm to 300 ppm overall). Phenocrystic K-feldspar from pHD, CPt, and CP all exhibit oscillatory zoning. Ba "spikes" are variable in concentration between individual grains, but those that are >10,000 ppm occur only in pHD and CPt K-feldspars. Ba abundances of interstitial groundmass K-feldspar grains are low, similar to concentrations of Ba in the rims of phenocrysts (<1600 ppm; not shown). This Ba zoning in the larger phenocrysts is mimicked by the elements Y (Figs. 7E, 7F) and Zn, whose core-to-rim transect shapes are near identical to those of Ba, although Y and Zn concentrations in one CP grain are close to those of pHD phenocrysts. The elements Sr (Figs. 7G, 7H) and Eu exhibit similar, but not identical, oscillatory zoning patterns as Ba, Y, and Zn. The core-to-rim transect patterns for these five elements correlate with the zoning patterns established with CL (i.e., lighter blue zones are coincident with higher Ba contents).

Rubidium concentrations do not follow the profile patterns defined by Ba, Y, and Zn, but show distinctions between K-feldspars from each unit. Rb distribution (Figs. 7I, 7J) is distinct between grains of different sizes (e.g., groundmass versus phenocrysts), much like Ba and corresponding elements. Rb varies little in subhedral grains characteristic of KCt, eHD, and eHDt, although Rb concentrations in the eHDt sample are higher than in the other units (Fig. 7I). Transects of K-feldspar phenocrysts typical of pHD, CPt, and CP have two distinct types of patterns for Rb concentration: (1) Rb is typically near constant at ~250 ppm in cores of these grains, where high-Ba spikes are common; whereas (2) Rb in the rims of these grains sharply increases where Ba continuously decreases, reaching between 450 and 600 ppm, depending on the unit.

Słaby et al. (2011), building on experimental and numerical modeling work by Perugini et al. (2002, 2003, 2008) and De Campos et al. (2008), pointed out that Ba, Sr, and Rb concentrations in K-feldspar are expected to show nonlinear behavior because they diffuse at different rates and thus have different concentration gradients when magma domains interact. Because Rb diffuses the fastest, it reequilibrates fairly quickly with the surrounding melt, which explains the near-constant Rb concentrations from core to rim in K-feldspar, whereas Ba is the slowest-diffusing element, and Sr diffuses faster than Ba but slower than Rb (Słaby et al., 2011). This is compatible with the fact that Ba and Sr are more likely to show "spikes" as they do in the K-feldspars of this study and thus better reflect changes in melt composition due to mixing.

Titanium concentrations follow a similar pattern to the K-feldspar growth zones as distinguished with the CL colors, but Ti concentrations are distinct in some units (Figs. 7K, 7L). K-feldspar in KCt ranges in Ti concentrations from ~60 to120 ppm, which is higher than Ti concentrations in eHD and eHDt K-feldspar grains that also follow simple zoning patterns. Phenocrystic K-feldspars in pHD, CPt, and CP follow a zoning pattern with minor oscillations, much like Ba and elements with similar behavior, but without any distinct differences between core and rim compositions.

PLAGIOCLASE MAJOR AND TRACE ELEMENT COMPOSITIONS

Anorthite (An) content in plagioclase from the different TIC units ranges markedly (Table 1) (see Supplemental Files 10 and 11 [footnote 1] for An contents and major oxide concentrations, respectively). The highest and widest range of values is from plagioclase in KCt (An_{50}–An_{18}). Plagioclase from eHD, eHDt, and pHD overlap in their ranges (An_{42}–An_{15}), which are slightly lower than that of KCt. Plagioclase compositions in CPt and CP are roughly identical in their ranges (An_{33}–An_{12}) and trend to the least-calcic plagioclase compositions in the TIC. While these An ranges encompass most plagioclase compositions in each unit, several cores are compositionally distinct from their surrounding grain. Examples include one eHD plagioclase core at An_{86} and multiple resorbed cores at >An_{40} in CP, CPt, and pHD. The latter types of cores are commonly bright green under CL and surrounded by sericite.

Trace element variation in plagioclase (Supplemental File 12 [footnote 1]) is plotted as a function of An content in Figure 8. Sr in KCt overlaps significantly in concentration with that in eHD and eHDt, with all three units containing Sr ≤1461 ppm in plagioclase (Fig. 8A). In contrast to Sr, trace elements such as light rare earth elements (LREEs; represented by Ce in Fig. 8B), Ba (Fig. 8C), and Ti (Fig. 8D) are highest in many KCt spots. KCt plagioclase notably contains as much as 700 ppm Ba and 130 ppm Ti, both of which are high concentrations compared with those of all other units. Several spots from the cores of eHD and eHDt plagioclase grains overlap with these values, but most are at lower trace element concentrations and An contents.

Figure 8 also demonstrates that plagioclase grains in CP and CPt overlap in Sr, Ce, Ba, and Ti compared with An. Most plagioclase from CP and CPt are distinct in terms of Sr and An compared to those from KCt, eHD, and eHDt, although compositions tend to converge at low An contents. Compared to the eHD-like trend, CP and CPt grains contain higher Sr values (as high as ~1700 ppm). Additionally, at any given Sr value <1500 ppm, CP and CPt grains contain lower An contents compared to KCt, eHD, and eHDt grains (Fig. 8A). Several cores at >An_{40} that are bright green under CL from CP plagioclases (along with one from CPt and one from pHD) plot at higher Sr concentrations (2000–3500 ppm). Two points from the core of one CP plagioclase occupy plot space defined by eHD and eHDt plagioclase An and Sr contents. Most CP and CPt plagioclase spots also have the lowest LREE values, with Ce typically <15 ppm (Fig. 8B). This range does not include high-An cores from CP, CPt, and pHD, which plot at a wide range of Ce values, or the core of one plagioclase with eHD-like An and Sr contents. With the exception of KCt spots, most TIC plagioclase are in the same range of Ba and Ti (<400 ppm Ba and ≤60 ppm Ti) (Figs. 8C, 8D).

PORPHYRITIC HALF DOME GRANODIORITE AND OVERLAP WITH EQUIGRANULAR HALF DOME AND CATHEDRAL PEAK COMPOSITIONS

It is noticeable that eHD and CP plagioclase have distinct ranges of An content, Sr, and LREEs that overlap only at the most evolved (lowest An and Sr) compositions. The pHD unit, which is spatially and temporally bracketed between the eHD and CP units, has plagioclase compositions that overlap eHD and CP compositional trends, as well as some that are intermediate between the two trends (Fig. 8). Plotting of individual plagioclase grains from different pHD samples (Fig. 9) demonstrates the heterogeneity of plagioclase compositions within the pHD and their relationship to those of the eHD and CP units. Two pHD samples, Y26 and Y31, contain only plagioclase grains plotting along an eHD trend ($An_{40–20}$, Sr at 500–1500 ppm, and Ce >12 ppm), while some grains from samples L6A and L77A only contain cores plotting within the eHD trend. Samples L6A, L77A, and L80 contain grains that mostly plot along a CP trend ($An_{30–15}$, Sr at 500–2500 ppm, and Ce <12 ppm). Sample L77A additionally contains a resorbed core with high Sr (~3000 ppm), similar to cores rarely observed in the CP. Additionally, multiple points from several pHD plagioclase grains plot within a zone between the characteristic eHD and

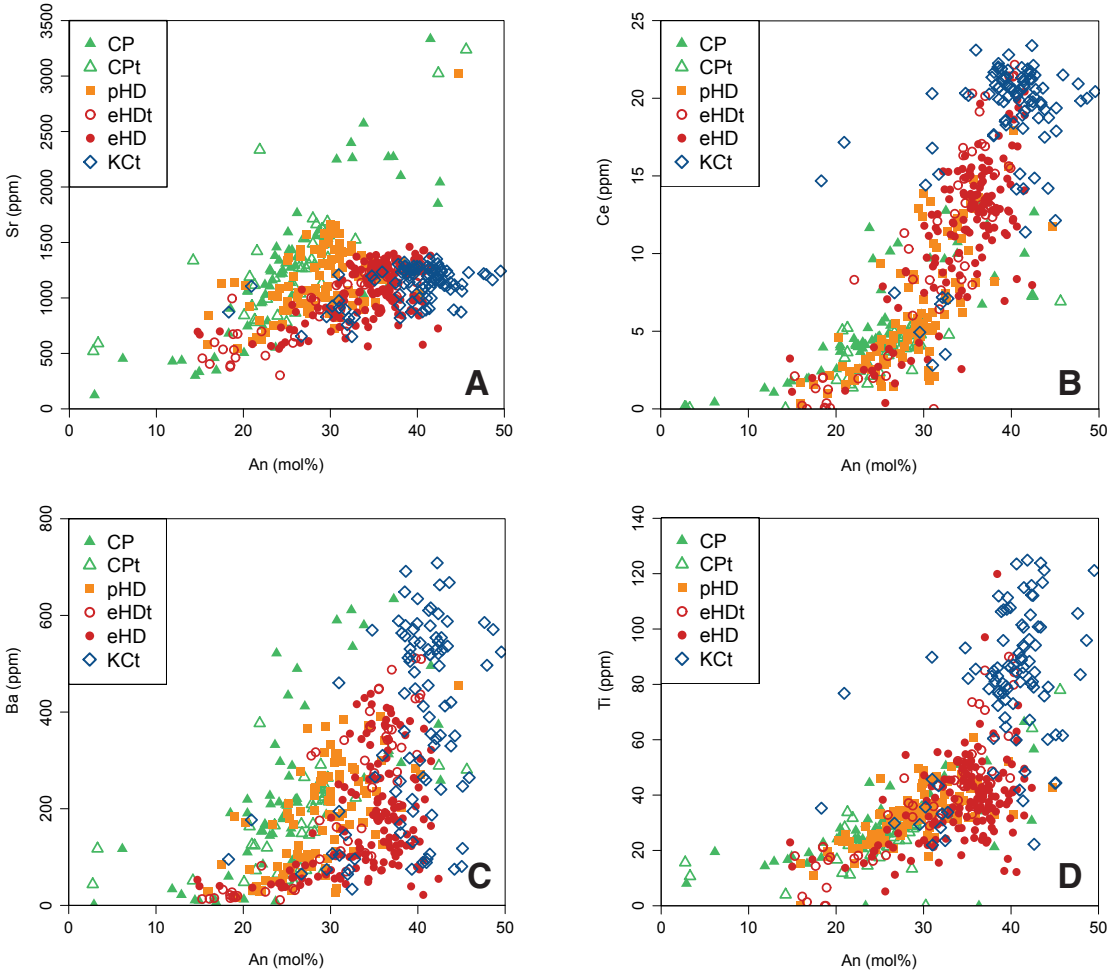

Figure 8. Binary plots comparing anorthite (An) content (mol%) in plagioclase with content of selected trace elements (ppm). Unit abbreviations: KCt—transitional zone between granodiorite of Kuna Crest (KC) and eHD; eHD—equigranular Half Dome Granodiorite; eHDt—transitional zone between eHD and pHD; pHD—porphyritic Half Dome Granodiorite; CPt—transitional zone between pHD and CP; CP—Cathedral Peak Granodiorite. (A) An versus Sr. (B) An versus Ce. (C) An versus Ba. (D) An versus Ti.

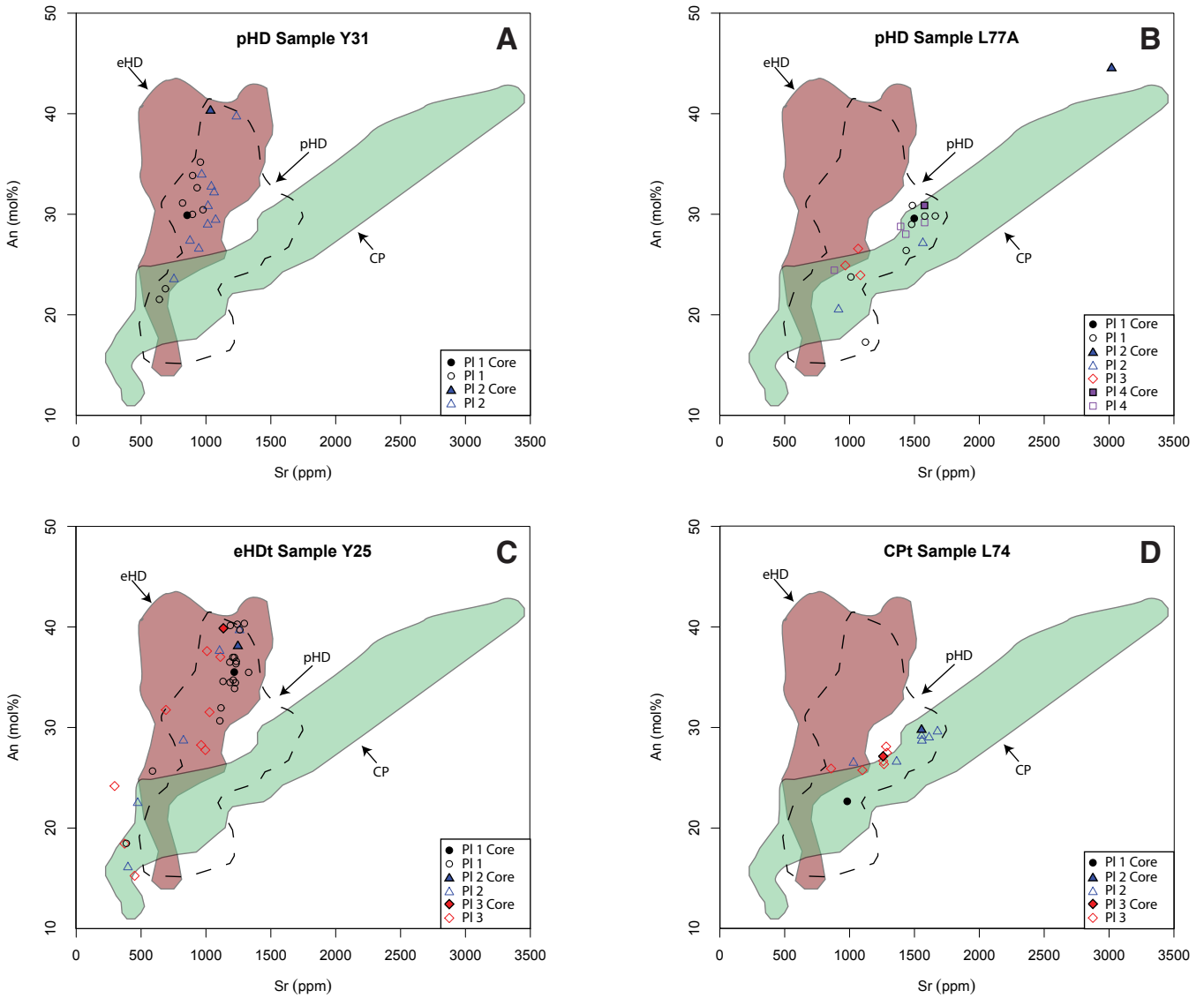

Figure 9. Geochemistry of plagioclase (Pl) grains from selected porphyritic Half Dome Granodiorite (pHD), transitional equigranular Half Dome Granodiorite (eHDt), transitional Cathedral Peak Granodiorite (CPt), and southern Half Dome (SHD) lobe samples (Economos et al., 2009) indicating units containing mixed populations of plagioclase. Maroon and green polygons represent all eHD and CP plagioclase, respectively; dashed black field represents all pHD plagioclase analyses. (A–D) Anorthite content (An) (mol%) versus Sr (ppm) in pHD sample Y31 near the pHD-CPt contact southeast of Tuolumne Meadows (A), pHD sample L77A between the eHD and CPt contacts near Evelyn Lake (B), eHDt sample Y25 (C), and CPt sample L74 (D). (E–H) Ce (ppm) versus Ba (ppm) in pHD sample Y26 near the eHDt-pHD contact in Lyell Canyon (E), pHD sample L6A near the pHD-CPt contact in Lyell Canyon (F), eHDt sample Y25 (G), and CPt sample L74 (H). (I) An (mol%) versus Sr (ppm) in SHD lobe sample REE007 (marginal equigranular granodiorite). (J) Ce (ppm) versus Ba (ppm) in SHD lobe sample REE007. (K) An (mol%) versus Sr (ppm) in SHD lobe sample REE005 (central granite). (L) Ce (ppm) versus Ba (ppm) in SHD lobe sample REE005. (*Continued on following two pages.*)

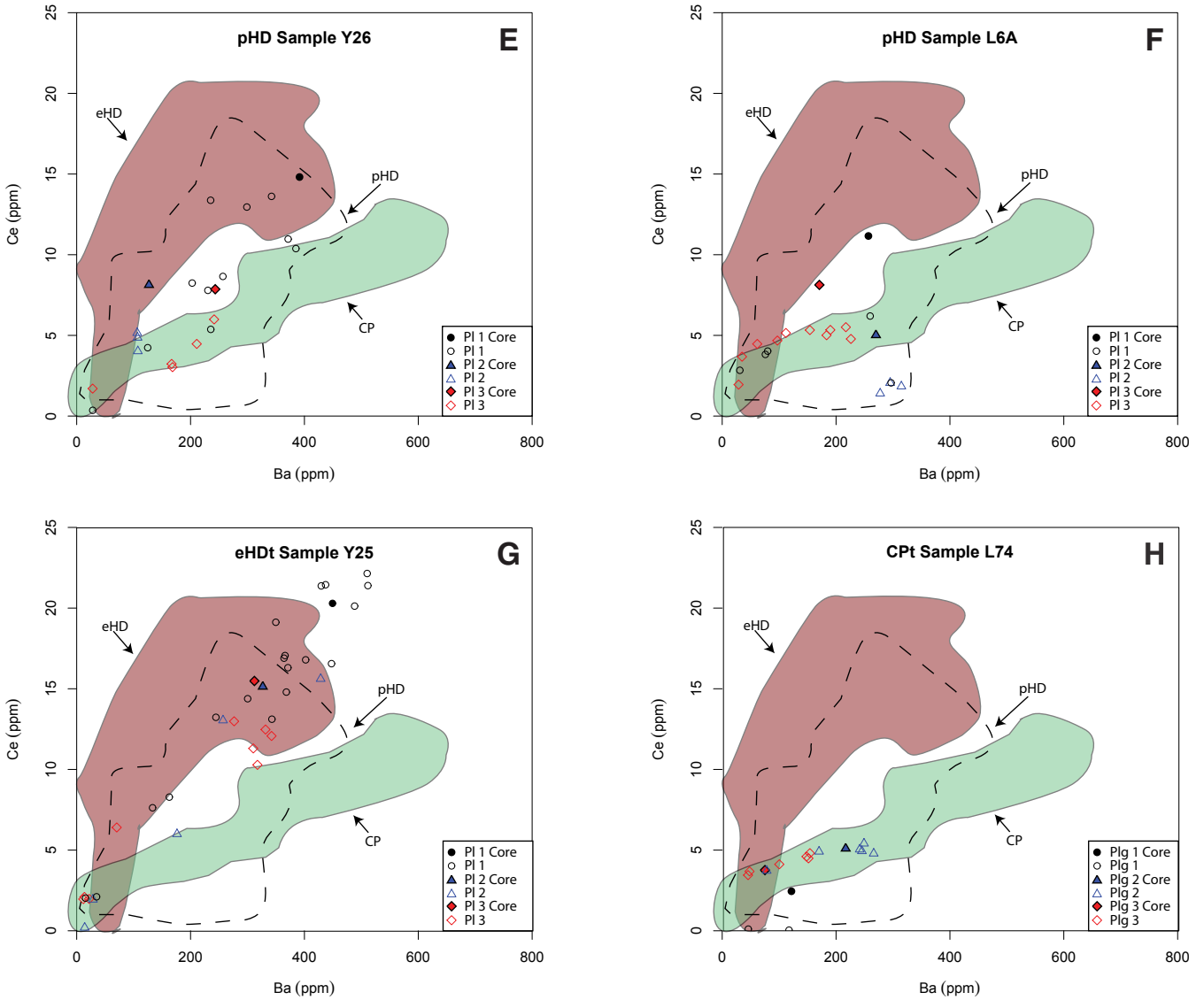

Figure 9 (*continued*).

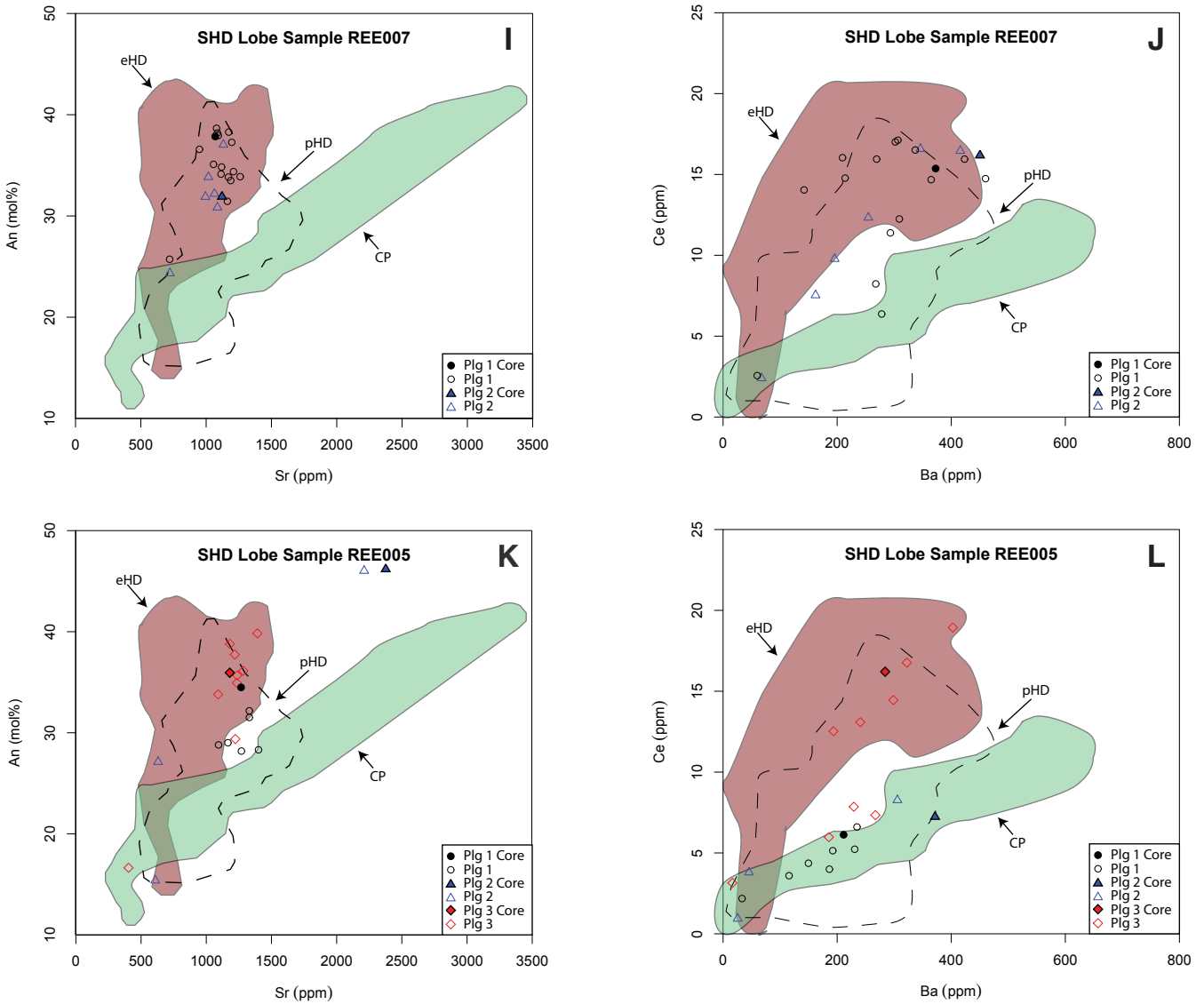

Figure 9 (*continued*).

CP trends in at least one plot (i.e., sample Y26 grains 1 and 3, and sample L6A grains 1 and 3). All pHD sample locations were near a contact with a neighboring transition to pHD (either eHDt or CPt), and all but one sample (Y31) contain plagioclase populations mimicking the compositions of the closest transition unit (and hence, the closest major unit) (Figs. 1, 9A, 9B, 9E, 9F).

FELDSPAR COMPOSITIONS OF THE SOUTHERN HALF DOME LOBE

While this study focuses on feldspars from the transition from the KC lobe to the main TIC complex, feldspars from the southern porphyritic Half Dome (SHD) lobe (Fig. 1; Economos et al., 2009) were also analyzed. These samples are included to compare the study region representing the main TIC with abundant field evidence for magma interaction between units with the SHD lobe, a zone separated from the main TIC body through extrusion into the host rock. The SHD lobe was previously interpreted to be slightly older than the pHD unit in the main TIC body and to have undergone less or no interaction with other TIC units at the emplacement level. Chemically, it is characterized by crystal fractionation (Economos et al., 2009; Memeti et al., 2010). Samples REE005 (central granite) and REE007 (marginal unit) from the SHD lobe were both analyzed for trace elements in feldspars and produced telling results.

Two K-feldspar grains from the marginal unit are approximately the same size and shape and have the same zoning pattern as those of eHD samples collected near the KC lobe. Likewise, Ba and Rb patterns in these K-feldspar grains mimic those of eHD grains. K-feldspar analyzed from the granitic unit in the center of the SHD lobe is small and interstitial like those from the groundmass in some pHD rocks in the main TIC. One grain analyzed plotted at low Ba and high Rb, much like the groundmass K-feldspar in the pHD.

Plagioclase in samples REE005 and REE007 (Figs. 9I–9L), like those in the rest of pHD in the main TIC, exhibit heterogeneity within the unit. Two grains from sample REE007 exhibit LREE, Sr, and An content ranges much like those of grains from eHD. The rim compositions of one grain, however, overlap with the CP trend when comparing An content with Sr. Sample REE005 contains plagioclase corresponding with both eHD and CP signatures, with all grains overlapping with the CP trend at some point in their growth history. The largest grain has a core composition with a high Ce concentration similar to that of eHD plagioclase, while the smallest two grains completely overlap with CP grains in Ce composition. The smallest grain contains a core with >2000 ppm Sr that is also bright green in CL.

PLAGIOCLASE CRYSTALLIZATION TEMPERATURES IN THE TUOLUMNE INTRUSIVE COMPLEX

Estimated crystallization temperatures for plagioclase were calculated using equation 2 from Caricchi and Blundy (2015). The experiments were conducted at 200 MPa and 720–1100 °C and calibrated to the Fish Canyon Tuff, a monotonous dacite compositionally similar to the TIC (Bachmann et al., 2002; TIC intruded at ~2–3 kbar: Ague and Brimhall, 1988). The temperature ranges for each unit are shown in Figure 10. Plagioclase grains from all units exhibit a wide range in temperature spanning between the estimated wet granite solidus at 670 °C (Johannes, 1984) and <1200 °C. Several points in each unit, except for the SHD samples, are <720 °C and even subsolidus temperatures, which are outside the calibration temperatures of Caricchi and Blundy (2015) and are thus mostly ignored. Suffice to say that these points, which also appear brown in CL, mostly correspond to plagioclase rim compositions and thus represent final low-temperature melts as expected. Most plagioclase grains, however, yield temperatures far above the estimated wet granite solidus (670 °C) and confirm the wide range of temperatures under which plagioclase crystallized in the TIC.

MELT COMPOSITIONS DETERMINED FROM PLAGIOCLASE COMPOSITIONS

The abundance of SiO_2 and CaO of melts in equilibrium with plagioclase cores from all TIC units were calculated using equations 2 and 3, respectively,

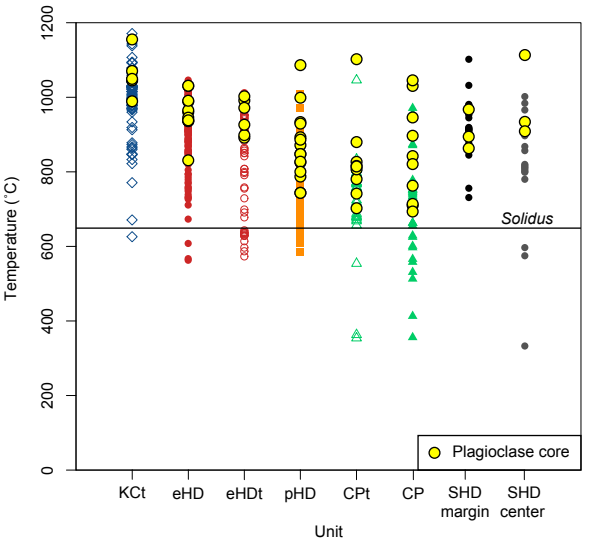

Figure 10. Calculated plagioclase crystallization temperatures (°C) for plagioclase from each Tuolumne intrusive complex unit. Units are Cathedral Peak Granodiorite (CP), transitional Cathedral Peak Granodiorite (CPt), porphyritic Half Dome Granodiorite (pHD), transitional equigranular Half Dome Granodiorite (eHDt), equigranular Half Dome Granodiorite (eHD), transitional Kuna Crest Granodiorite (KCt), and southern Half Dome Lobe (SHD) margin and interior. Temperatures were calculated using equation 2 from Caricchi and Blundy (2015).

from Scruggs and Putirka (2018). The results indicate that calculated melt SiO_2 contents are consistently higher than the SiO_2 contents analyzed in the bulk rocks (Fig. 11A). Likewise, calculated CaO content is consistently lower than the analyzed content of whole-rock samples (Fig. 11B). Comparisons of CaO and SiO_2 melt compositions for each unit suggest that plagioclase crystallized from rhyolitic or rhyodacitic melts in each unit that were more silicic and less calcic than the bulk rock compositions. The range of SiO_2 compositions is slightly wider in CPt and CP units, where some rim compositions are $<An_{20}$ (Figs. 11A, 11B).

Selected trace element compositions of melt in equilibrium with plagioclase cores were determined using distribution coefficients (K_d) from Padilla and Gualda (2016) and Iveson et al. (2018) for rhyolite and rhyodacite, respectively, and are compared with corresponding analyzed whole-rock values (Figs. 11C–11J). K_d values from these studies were used because they represent compositions similar to those of TIC whole rocks and the calculated melts. Only melt compositions in equilibrium with plagioclase cores are shown because they are more likely to represent original melts before significant fractionation occurred that would have either elevated or depleted trace elements at later stages of crystallization.

The most consistent results observed using the different K_d values for both melt compositions are observed in Sr and Rb. Calculated melt Sr using the K_d for rhyolite (K_d = 14) (Padilla and Gualda, 2016) yields values that are consistently lower than the corresponding whole-rock sample analyses for all units (Fig. 11C). Melt calculated using a K_d for rhyodacite (K_d = 3.31) (Iveson et al., 2018), like calculated rhyolitic melt, generally indicates less Sr than whole rock analyses (Fig. 11D). KCt, eHD, eHDt, pHD, and CPt calculated rhyodacitic melt Sr compositions are generally lower than whole-rock analyses, but in CP, Sr composition is widely variable and overlaps with that of CP whole-rock samples. Additionally, four cores from pHD, CPt, and CP yield higher calculated melt Sr than whole-rock values. The use of K_d values for rhyolitic and rhyodacitic melts demonstrates a similar pattern in Rb. Rhyolitic (K_d = 0.018) and rhyodacitic melt (K_d = 0.02) contain Rb at lower concentrations than whole-rock

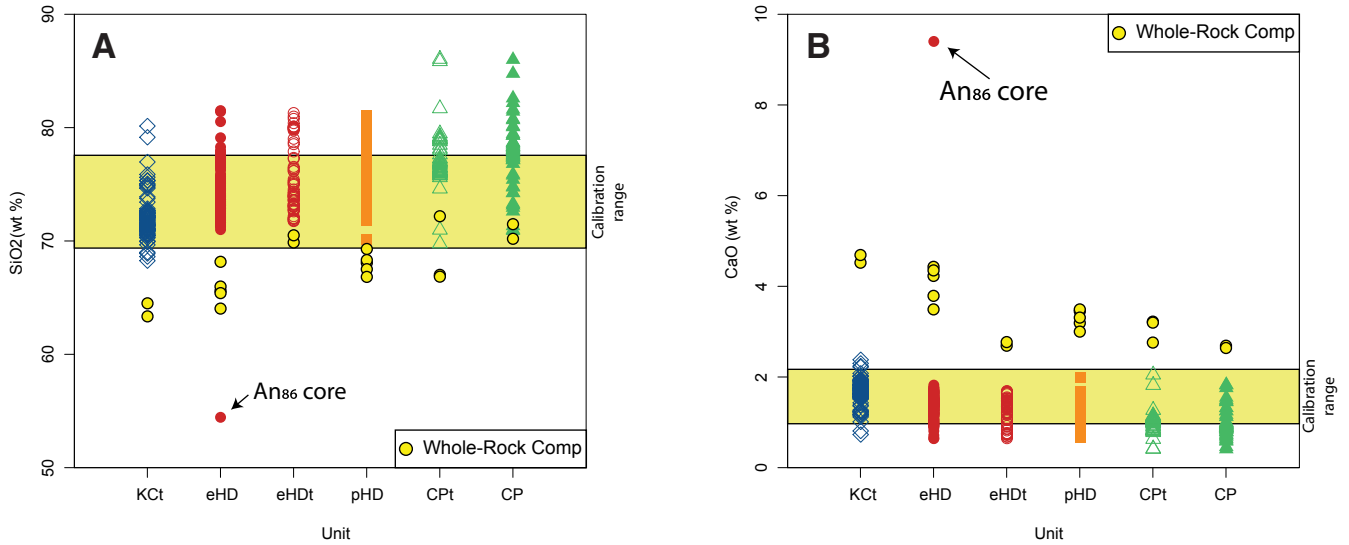

Figure 11. (A, B) Calculated SiO_2 (wt%) (A) and CaO (wt%) (B) compositions for melt in equilibrium with Tuolumne intrusive complex plagioclase compared to whole-rock analyses. Units are Cathedral Peak Granodiorite (CP), transitional Cathedral Peak Granodiorite (CPt), porphyritic Half Dome Granodiorite (pHD), transitional equigranular Half Dome Granodiorite (eHDt), equigranular Half Dome Granodiorite (eHD), and transitional Kuna Crest Granodiorite (KCt). Major oxide compositions were determined using equations 2 and 3, respectively, from Scruggs and Putirka (2018). A plagioclase core from eHD measured at An_{86} (measured in molar percent) is labeled as such (C–J) Trace element compositions versus calculated SiO_2 (wt%) of whole-rock samples (colored fields) compared to calculated trace element compositions of melts in equilibrium with plagioclase (points). (C) Calculated Sr (ppm) using the rhyolite K_d = 14 from Padilla and Gualda (2016). (D) Calculated Sr (ppm) using the rhyodacite K_d = 3.31 from Iveson et al. (2018). (E) Calculated Rb (ppm) using the rhyolite K_d = 0.018 from Padilla and Gualda (2016). (F) Calculated Rb (ppm) using the rhyodacite K_d = 0.02 from Iveson et al. (2018). (G) Calculated Ba (ppm) using the rhyolite K_d = 4.50 from Padilla and Gualda (2016). (H) Calculated Ba (ppm) using the rhyodacite K_d = 0.25 from Iveson et al. (2018). (I) Calculated Zn (ppm) using the rhyolite K_d = 0.155 from Padilla and Gualda (2016). (J) Calculated Zn (ppm) using the rhyodacite K_d = 0.14 from Iveson et al. (2018). The calibration range of Scruggs and Putirka (2018) is depicted in plot backgrounds in yellow. comp—composition. (*Continued on following two pages.*)

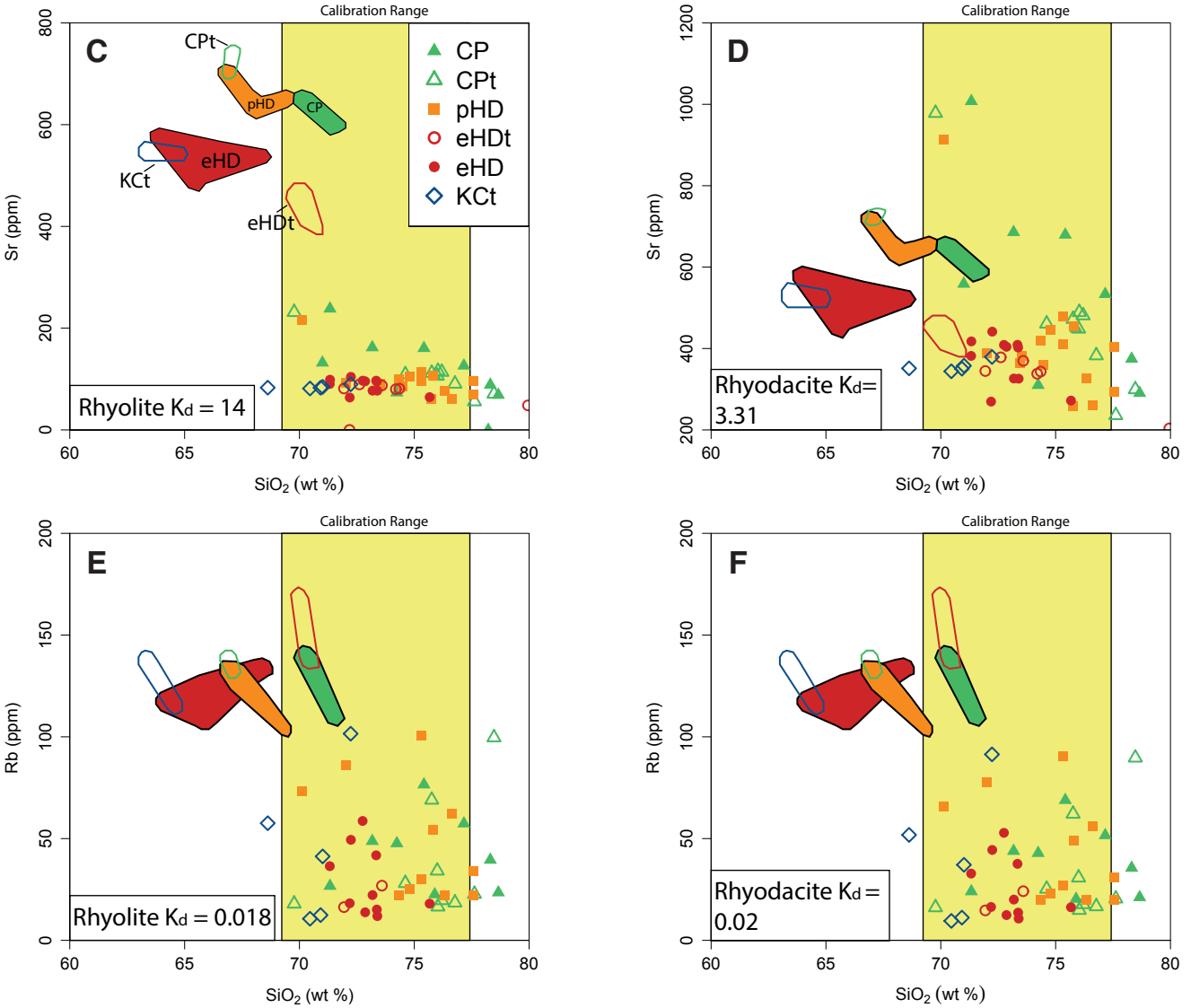

Figure 11 (*continued*).

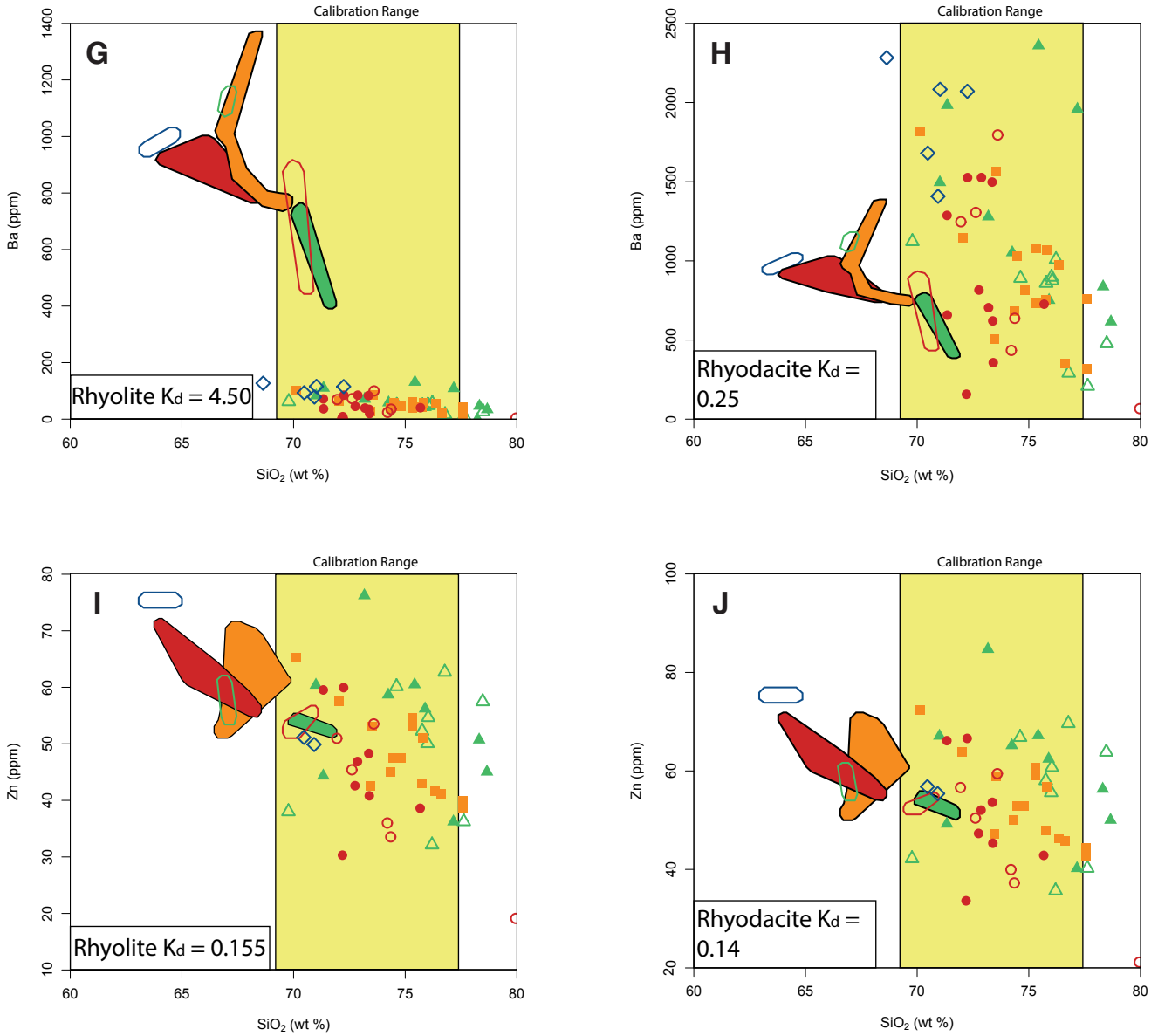

Figure 11 (*continued*).

analyses for all units (Figs. 11E. 11F). Results from both of these elements are consistent with mineral accumulation.

The trace element Ba yields variable results between rhyolitic and rhyodacitic melts due to significant differences in K_d values. Whole-rock Ba contents are consistently higher than calculated melt using rhyolitic K_d values for each unit (K_d = 4.50). Rhyodacitic melt Ba (K_d = 0.25), however, varies widely in how it compares to whole-rock Ba depending on the unit. KCt melt contains higher Ba than the corresponding whole rocks, as do several points from eHD, eHDt, pHD, and CP. Apart from KCt and CP, most calculated melt Ba compositions are similar to corresponding whole-rock compositions. CP exhibits a wide variation, with over half of melt compositions plotting at higher Ba than whole-rock values.

Zinc is similar for rhyolitic and rhyodacitic melt compositions due to similar K_d values for Zn in plagioclase (K_d = 0.16 and K_d = 0.14, respectively). The calculated melt generally forms a negative linear trend with the whole-rock compositions (i.e., lower Zn with higher SiO_2) (Figs. 11I, 11J). Much like Ba, Zn compositions in melt vary between units in how they compare with corresponding whole-rock compositions. Using both K_d values, Zn in KCt melt is lower than in KCt samples, and Zn compositions in eHD, eHDt, and pHD melt overlap with whole-rock compositions. Both CPt and CP exhibit wide ranges in melt Zn composition and are thus variable in how they compare with whole-rock compositions.

DISCUSSION

Crystal Recycling Patterns in the Kuna Crest Lobe–TIC Main Body Transition

Characteristics of K-feldspar and plagioclase populations in the different units and inter-unit transitions of the southeastern part of the TIC are summarized in Tables 2 and 3, respectively. These feldspar populations are shown schematically in Figure 12, illustrating that feldspar populations in TIC units can be tracked and identified across unit boundaries. Feldspar populations are determined based on size, petrographic features in thin section and under CL, and geochemical characteristics. In the case of K-feldspar, original Or content calculations suggest that perthite exsolution may have had only a minimal effect on Or composition, as also shown by others (Johnson and Glazner, 2010; Glazner and Johnson, 2013), but the effect is also rather difficult to fully evaluate and thus needs further study. The results from the geothermometer by Caricchi and Blundy (2015) suggest that plagioclase crystallization extended from temperatures >1000 °C to the solidus (Fig. 10). As such, plagioclase was capable of recording mixing between magma batches and, if it occurred, recycling of older into younger magmas. Tracking the spatial extent of these populations within and across unit boundaries helps to determine what these compositionally and texturally different TIC units represent; to determine to what degree they are (1) separate, individual magmas with distinct compositions, (2) mixed magmas, or (3) fractionates of other preserved magma bodies in the system; and to determine magma mush body size and extent at different times during TIC evolution.

Relationship between Transitional Kuna Crest and Equigranular Half Dome Granodiorites

In both KCt and eHD, plagioclase is euhedral, suggesting that it grew unimpeded by other crystals in a magma that was capable of mixing into adjacent units. All plagioclase grains analyzed from the transitional KCt unit have higher An, Ti, Ba, and LREE contents than eHD and thus grew from a slightly more primitive melt than eHD did (Fig. 8). However, both KCt and eHD are along a fractionation array defined by relatively narrow ranges in Sr (542–1461 ppm) and broader ranges in LREEs and Y (e.g., 0.38–20 ppm Ce in eHD), suggesting

TABLE 2. SUMMARY OF K-FELDSPAR POPULATIONS IN THE TUOLUMNE INTRUSIVE COMPLEX (TIC)

K-feldspar population	Petrographic characteristics	Geochemical characteristics	TIC unit(s)
1	Subhedral to anhedral; ~1 mm across; inclusions uncommon and lack crystallographic orientation	Simple Ba, Y, and Zn zonation; non-zoned Rb	eHD
2	Euhedral; as long as 4 cm; abundant crystallographically oriented inclusions of plagioclase, biotite, hornblende, and titanite	Oscillatory Ba zonation as high as ~1.8 wt%; gradual to sharp increases in Rb from interior to rim	pHD, CPt
3	Euhedral; as long as 4 cm; crystallographically oriented plagioclase inclusions; mafic inclusions rare compared to population 2	Same Ba zonation and Rb pattern as population 2; Ba concentrations at maximum ~1 wt%	CP
4	Subhedral to anhedral; ~1 mm across; inclusions uncommon and lack crystallographic orientation	Simple Ba, Y, and Zn zonation; non-zoned Rb; Ti and light rare earth elements enriched relative to population 1	KCt
5	Euhedral to subhedral; ~1 cm across; single quartz and plagioclase inclusion “rings” present in some grains	Mostly simple Ba zonation with minor oscillations; non-zoned high Rb	eHDt

Note: Units are Cathedral Peak Granodiorite (CP), transitional Cathedral Peak Granodiorite (CPt), porphyritic Half Dome Granodiorite (pHD), transitional equigranular Half Dome Granodiorite (eHDt), equigranular Half Dome Granodiorite (eHD), and transitional Kuna Crest Granodiorite (KCt).

TABLE 3. SUMMARY OF PLAGIOCLASE POPULATIONS IN THE TUOLUMNE INTRUSIVE COMPLEX (TIC)

Plagioclase population	Petrographic characteristics	Geochemical characteristics	TIC unit(s)
1	Euhedral; grains commonly exhibit minor oscillatory zonation; mafic inclusions uncommon but may be crystallographically oriented around grain's outer interior	An_{50}–An_{15}, Sr at 500–1500 ppm, Ce at 0.4–22 ppm	KCt, eHD, eHDt, pHD, CP
2		An_{32}–An_{14}, Sr at 500–1800 ppm, Ce at 0.3–18 ppm	pHD
3		An_{30}–An_{14}, Sr at 300–2000 ppm, Ce at 0–13 ppm	CP, CPt
4	Resorbed core; commonly commonly bright green in cathodoluminescence	An_{45}–An_{40}, Sr at >2000 ppm	pHD, CPt, CP
5	Resorbed core in a single eHD plagioclase grain	An_{86}	eHD

Note: Units are Cathedral Peak Granodiorite (CP), transitional Cathedral Peak Granodiorite (CPt), porphyritic Half Dome Granodiorite (pHD), transitional equigranular Half Dome Granodiorite (eHDt), equigranular Half Dome Granodiorite (eHD), and transitional Kuna Crest Granodiorite (KCt). Plagioclase anorthite (An) content subscript are in molar percent.

that the plagioclase compositions from KCt and eHD could be related to each other through fractionation (Figs. 8A, 8B). Whether plagioclase mixing between KC and eHD took place prior to fractionation is unclear because the plagioclase populations in KCt and eHD are compositionally very similar, but other data sets discussed below have established evidence for mixing between KC and eHD to form KCt.

Potassium-feldspar grains in KCt and eHD appear similar petrographically and exhibit the same type of zoning (Figs. 5A, 6A). Hybridization of different K-feldspar populations between KC and eHD, however, cannot be established for the following reasons: (1) K-feldspars in both units are largely subhedral to anhedral and of low modal abundance, suggesting that they formed relatively late with little melt present in the magma and would therefore not have been able to remobilize (e.g., by incorporation into new batches of magma); (2) additionally, while Ba, Zn, Y, and Rb concentrations for KC and eHD K-feldspars are in the same range, Ti, La, and Ce in KCt K-feldspars are higher than those recorded in any eHD K-feldspar (Fig. 7K). K-feldspar in KCt and eHD are thus determined to have grown in situ and separately from each other in their respective magma bodies.

Relationship between Equigranular Half Dome and Transitional Equigranular Half Dome Granodiorites

Whole-rock geochemical analyses of eHDt show that this unit is a low-silica granite, rather than a granodiorite as expected from hybridization between eHD and pHD granodiorites (Fig. 3). Additionally, comparisons of the trace elements Sr and Y against SiO_2 show that eHDt is depleted in Sr and Y relative to KCt and eHD (Fig. 4). Plagioclase from eHDt are geochemically similar to, and exhibit the same characteristics as, eHD grains (Figs. 9C, 9G) or are slightly more trace-element depleted (Fig. 8). Analyzed K-feldspars are euhedral, like pHD

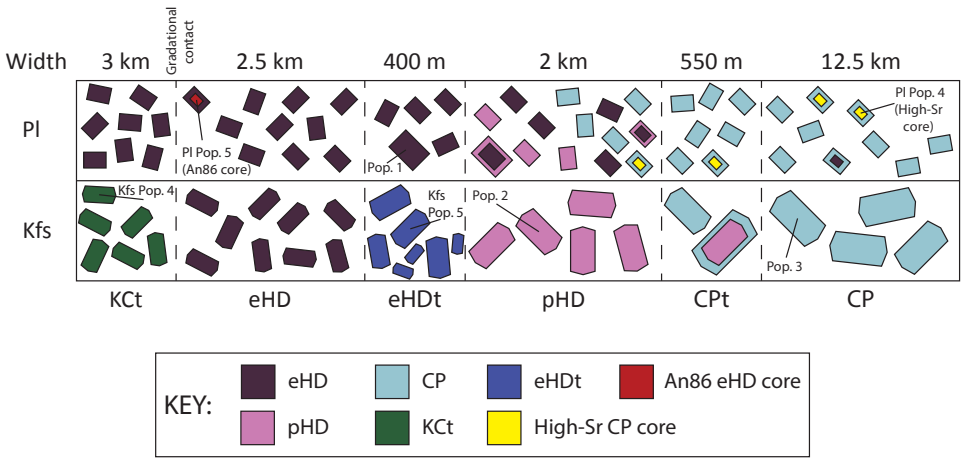

Figure 12. Schematic illustration of plagioclase and K-feldspar population distributions across all major Tuolumne intrusive complex units, including gradational transitions. Units are Cathedral Peak Granodiorite (CP), transitional Cathedral Peak Granodiorite (CPt), porphyritic Half Dome Granodiorite (pHD), transitional equigranular Half Dome Granodiorite (eHDt), equigranular Half Dome Granodiorite (eHD), and transitional Kuna Crest Granodiorite (KCt). Each feldspar population is abbreviated as "Pop. #", based on characteristics described in Tables 2 and 3. A plagioclase core from eHD measured at An_{86} (measured in molar percent) is labeled as such. Width in this figure refers to the maximum horizontal distance of each unit in this study's field area.

K-feldspar phenocrysts, but lack extensive oscillatory Ba zoning. These grains are geochemically distinct from those of both eHD and pHD, with consistently more evolved compositions containing higher Rb concentrations than eHD grains and pHD cores (Figs. 6B, 7I, 7J). Simple Ba zoning in one grain coincides with core-to-rim zoning seen in CL and round quartz inclusions marking the initiation of the rim zone, which suggests the presence of a highly evolved, quartz-saturated melt during rim growth. The combination of petrography and feldspar compositions suggests that eHDt is composed of fractionated eHD magma and does not represent a zone of magma mixing between the adjacent eHD and pHD units. The evidence that eHDt fractionated from eHD suggests that other high-silica bodies in eHD, such as irregular leucogranite bodies and aplites, are likely fractionates of eHD as well (Bateman and Chappell, 1979; Economos et al., 2009; Coleman et al., 2012; Memeti et al., 2014).

Porphyritic Half Dome Granodiorite and Its Relationship to Equigranular Half Dome and Cathedral Peak Granodiorites

Plagioclase in pHD samples from different portions of the east-west transects is petrographically similar but varies geochemically among samples (Figs. 9A, 9B, 9E, 9F). This heterogeneity, when compared to the eHD or CP, is indicative of mixing across TIC units during pHD emplacement, and involved plagioclase from eHD and CP magmas. A third plagioclase population in pHD containing interiors and cores intermediate to eHD and CP suggests that some grains either nucleated or continued to grow in this hybrid magma. Wallace and Bergantz (2002) used a wavelet-based correlation technique on backscattered electron images of plagioclase from one sample each from pHD and CP to reveal a complex plagioclase transport history within the pHD unit and at least two different plagioclase populations, consistent with our trace element results and interpretations.

Conversely, oscillatory-zoned K-feldspar phenocrysts abundant across pHD are difficult to distinguish from one another (Fig. 6C). Most possess growth zones containing repeated sharp and high spikes in Ba (as high as almost 2 wt%) followed by gradual Ba decreases (Figs. 7B, 7D). We thus interpret that K-feldspar phenocrysts in pHD are all compositionally similar and do not show evidence of recycling from either eHD or CP.

The presence of mixed plagioclase populations geochemically similar to those of eHD and CP suggests that pHD is a hybrid of the two units (Fig. 9). An evolved eHD magma (preserved as mushy, *granitic* eHDt) and a more primitive CP magma (where present, preserved as CPt) appear to represent the two end-member compositions. It is also evident that pHD did not form in one magma mixing event but formed by gradual hybridization of fractionated eHD with increasingly more CP-like magmas toward the TIC interior. The plagioclase shows that the pHD closest to eHD has the greatest eHD affinity (Figs. 1, 9) (and thus eHD material recycling), and the pHD closest to CP contains the greatest CP component (Figs. 9B, 9F). Because only plagioclase exhibits multiple mineral populations but the small K-feldspar phenocrysts are similar across the entirety of the pHD, mixing between eHDt and CPt occurred before crystallization of these K-feldspar phenocrysts. The oscillatory Ba, Sr, Y, and Zn zoning in pHD K-feldspar phenocrysts is attributed to repeated replenishment by CP magma batches, as has been suggested previously (e.g., Moore and Sisson, 2008; Memeti et al., 2014).

Relationship between Cathedral Peak and Transitional Cathedral Peak Granodiorites

K-feldspar phenocrysts in CPt and CP (~5 cm) exhibit oscillatory zoning of Ba, concentrations of which in CP do not exceed 10,500 ppm (Fig. 7D). Some K-feldspar in CPt show inheritance from pHD. One phenocryst containing abundant hornblende and biotite inclusions, approximately the same size as typical mineral inclusion–rich pHD phenocrysts, contains as much as 18,000 ppm Ba, which is typical of some pHD K-feldspar phenocrysts (Fig. 7D). This grain is similar in Ba, Y, Sr, and Rb rim compositions to those of other CPt phenocrysts (Figs. 7D, 7F, 7H, 7J). This pattern is not observed in any other phenocrysts (whose lowest concentrations of Ba, Y, and Sr are reached at ≤1 mm from the rim). Both observations suggest that this phenocryst grew in pHD, was recycled into CP magma, and continued growth in a melt low in Ba, Y, and Sr and high in Rb. Such K-feldspar phenocryst mixing is also required to support zircon inclusion ages acquired from CPt megacryst sample L74 by Chambers et al. (2020), which yielded older, pHD zircon ages in the K-feldspar megacryst core and younger, CP ages from the rim, amounting to a 0.5 m.y. age difference between core and rim growths.

While K-feldspar in CPt suggests that the unit is a hybrid, plagioclase populations within CP and CPt are geochemically identical (Fig. 8), indicating that they grew from the same melt or similar melts (Figs. 8, 9D, 9H).

Cathedral Peak Plagioclase

The plagioclase populations of CP are noticeably more heterogeneous than in eHD, but all element concentrations at the rims are low relative to cores, reflecting the final crystallization of these grains in increasingly more evolved melt. Most CP grains define an approximately linear trend, with variable Sr, low An content, and low LREEs compared with the eHD trend (Figs. 8A, 8B). The cores of several grains are resorbed (Fig. 6D); these cores are consistently higher than other CP spots in Sr (2000–3500 ppm) and An (~An_{40}) and display variable and high LREE values. Such cores have not been observed in eHD. These features indicate that the resorbed cores crystallized from CP-like melts that were less evolved than CP melts typical of the level of emplacement. Two analyses of a plagioclase core display relatively high An values and LREEs but also low Sr contents, all of which are similar to eHD plagioclase. Comparison of this core with other plagioclase data from the TIC suggests that it is an antecryst from eHD magma that transferred into the CP, or alternatively that it is relict from an early mixing event.

Insight for the Formation of the Porphyritic Half Dome Granodiorite from the Southern Half Dome Lobe and Implications for Lobe Formation

Plagioclase from the marginal (sample REE007) and central units (sample REE005) of the southern Half Dome (SHD) lobe, which intruded into the host rocks of the TIC and away from other TIC units, yields characteristic pHD-like compositions. The marginal unit has a greater eHD affinity than the more CP-like central unit (Figs. 9I–9L). Additionally, bulk-rock Sr and Y compositions of SHD lobe samples plot along trends defined by pHD, CPt, and CP samples. This observation not only supports the hybrid nature of the pHD unit but also highlights the gradual increase in CP affinity from the older lobe margins to the younger interior (~400 k.y. difference in crystallization age; Memeti et al., 2010). This requires that the pHD lobe does not represent a simple, fully isolated magma body that formed due to simple fractional crystallization (Economos et al., 2009), but rather may represent a type of conduit. The majority of the lobe experienced gradual in-mixing of more CP-type magma over time to form the increasingly more evolved SHD lobe units toward its interior, prior to fractional crystallization of the leucogranitic lobe core. This conclusion also emphasizes the incremental nature of CP and eHDt magmas mixing to form pHD in the main study area.

Comparisons with Other Single-Mineral TIC Data

Interpretations of plagioclase analyses from KCt and eHD agree with interpretations of analyses of hornblende in KC and eHD (Barnes et al., 2016b). Our finding that eHD contains a single, dominant plagioclase population agrees with the single hornblende population described by Werts et al. (2020). Both minerals suggest that eHD (especially away from contacts) did not significantly mix with the adjacent TIC magmas. Where our results differ is in KCt, where hornblende populations from both KC and eHD are present. Petrographic characteristics of biotite and hornblende and whole-rock isotopes also suggest that KCt formed from the mixing of KC and eHD magmas (Barnes et al., 2016b; Memeti et al., 2010, 2014). One possible explanation as to why hornblende and plagioclase differ in whether they show mineral mixing into KCt is that KC (whose plagioclase grains were not examined in this study) and eHD contain similar plagioclase grains that cannot be distinguished from one another. In such a case, mixing between the two units may have occurred, but the grains are geochemically not distinguishable. Alternatively, the KC portion of the mixture was dominantly melt rich and contained small hornblende crystals but left (perhaps larger) plagioclase crystals behind in a cumulate in the KC lobe.

The greater abundance of mixed plagioclase populations in younger units (i.e., pHD and CP) agrees with the features of other TIC minerals described in previous studies, such as zircon. Both xenocrystic and particularly antecrystic zircons are increasingly more abundant toward the interior (pHD, CP) of the TIC (Miller et al., 2007; Memeti et al., 2014; Paterson et al., 2016). The Chambers et al. (2020) U-Pb geochronology study on zircons from cores and rims of two CPt megacrysts further confirms that pHD megacrysts (and their zircon inclusions) were recycled into younger CPt magmas, where they grew to megacrystic size. Paterson et al. (2016) also noted the presence of Half Dome hornblende-shaped and hornblende-sized biotite clots in CP and the presence of CP materials in the Johnson Granite Porphyry. These few examples all demonstrate that starting from the late KC stage, each younger TIC unit recycled older TIC materials during its incremental emplacement.

Implications for Pluton Emplacement and Time-Dependent Evolution Models

One of the most crucial aspects of this study is the implications that gradational contacts and feldspar mixing identified in the southeastern part of the TIC have for models of pluton emplacement and post-emplacement evolution. Previous studies described contact relationships between the TIC units in other locations in the eastern region of the TIC (Memeti et al., 2010, 2014; Žák and Paterson, 2005; Paterson et al., 2016). At Fletcher Peak to the south of our field area and Sawmill Canyon to the north, Paterson et al. (2016) showed that some TIC units are missing. These missing units are typically replaced by what the authors identified at the outcrop scale as hybrids that cut across older units. CP in these areas was identified as forming mostly sharp contacts with the older units, greatly contrasting with the continuous CPt unit identified in the area studied here. The regions where sharp contacts are exposed are likely locations where older units did not have enough melt present for interunit mixing, resulting in loss of materials through stoping and possible vertical displacement (Paterson and Fowler, 1993).

Crystal Mixing during Incremental Assembly and Magma Interconnectivity

A schematic illustration of the TIC formation at or near the emplacement level (Fig. 13) shows magma mixing as especially prevalent during formation of the hybrid pHD unit by mixing of evolved eHD magmas with CP magmas. This mixing is best illustrated by the presence of three types of plagioclase: those with features of eHD, those with features of CP, and those which occur specifically in pHD. This relationship indicates that eHD and CP magmas could thoroughly mix, leaving a hybrid magma capable of crystallizing the third plagioclase type. The fact that pHD becomes more CP-like inward, including in the SHD lobe, also suggests increasing proportions of incrementally injected CP magma toward the interior of the complex with time at or slightly below the emplacement level.

Furthermore, the presence of pHD-type K-feldspar (i.e., a phenocryst with a >1 wt% Ba core and protracted ~3000 ppm Ba rim compositions) in CPt indicates that emplacement of the CP magmas into older units was long lived. The 0.5 m.y. age difference between core and rim zircon ages from two K-feldspar megacrysts from the CPt unit confirm pHD-CP interconnectivity (Chambers et al.,

2020). The nature of this interconnectivity depends on whether this age difference reflects continuous or punctuated growth of the megacrysts. Continuous growth from core to rim would indicate the length of time during which pHD and CPt magmas were capable of mixing and interacting via melt, while punctuated growth would mark the time interval between times of crystallization of the pHD core and CP rim. Considering that the entire southeastern section of the TIC at the transition to the KC lobe is also characterized by gradational contacts (Fig. 1) and broad hybrid zones between major units (KCt, CPt) or zones of fractionated magmas (i.e., eHDt), all of which extend many kilometers along the strike of a contact indicating melt interconnectivity between at least two adjoining units, we consider continuous K-feldspar growth to megacrystic size over 0.5 m.y. quite likely. In this scenario, the intrusion of CP magma into mushy pHD magma was sufficient to disrupt the pHD mush and entrain K-feldspar into CPt. To determine how likely mixing in a magma mush is and the degree to which magmas hybridize, Schleicher and Bergantz (2017) used discrete element method–computational fluid dynamics simulations of individual crystals in a magma mush. They concluded that even a single open-system mixing event in crystal-rich magma mush could produce a diverse crystal cargo due to the fluidization of the mush in the mixing volume ("mixing bowl").

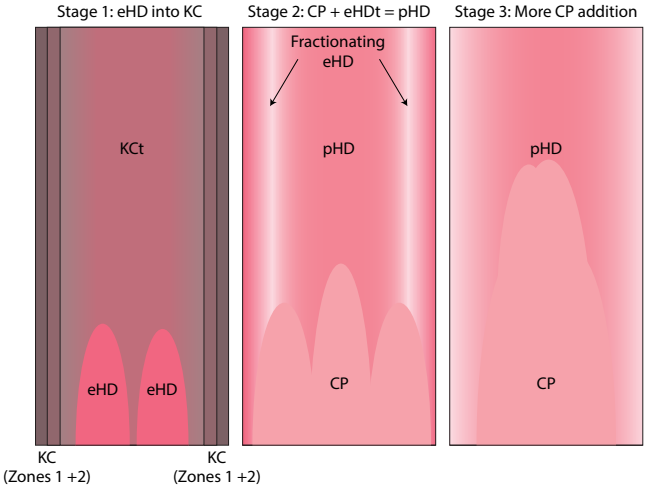

Figure 13. Schematic overview of a vertical cross-section of the Tuolumne intrusive complex (TIC) illustrating major magmatic events forming the TIC near the emplacement level, consisting of: KCt formation from mixing of the youngest KC zone and eHD (stage 1), pHD formation from incremental mixing of eHDt (fractionated eHD) and CP (stage 2), and continued incremental addition of CP magma into pHD. Units defined in Figure 12 caption. Cartoon is not to scale.

Calculations of Melt Compositions in Equilibrium with Plagioclase

Calculations of melt compositions in equilibrium with TIC plagioclase cores are supportive of mineral accumulation and melt loss during the hypersolidus evolution of the TIC. Calculations of SiO_2 and CaO content in the melt in equilibrium with plagioclase cores demonstrate that much of the plagioclase formed from rhyolitic melts that were more silicic and less calcic than the bulk compositions of the granodioritic rocks, a conclusion also reached by Werts et al. (2020) based on hornblende compositions and by Barnes et al. (2019) from comparisons of hornblende zoning and zircon saturation. Calculated trace element compositions of the melt from which plagioclase cores crystallized are also distinct from bulk-rock compositions (Fig. 11). While we understand that trace element concentrations can be affected by the absence or presence of competing minerals, variations in diffusion rates, magma mixing, and a lack of homogenization in magma domains, the patterns we observed in this study are more than just minor data-point scatter or noise and are consistent with the SiO_2 and CaO calculations. These data are consistent with the interpretation that bulk-rock compositions represent magmas that have accumulated crystals (Barnes et al., 2016b, 2020; Werts et al., 2020).

CONCLUSIONS AND IMPLICATIONS

The results of this study demonstrate that mixed mineral populations are not only present within the TIC but increase in abundance toward interior units. These trends in mineral mixing indicate melt-present interactions within and across unit boundaries. Such mixing at the emplacement level, combined with widespread evidence for post-mixing melt loss, would not have been possible if emplacement were by rapidly solidified magma pulses. These results argue against the emplacement of the TIC as a series of sills or dikes (Glazner et al., 2004; Bartley et al., 2008, 2018; Coleman et al., 2004, 2012).

Emplacement of the TIC started as distinct, sheet-like bodies in the marginal, older KC, but subsequent batches of magma gradually coalesced into increasingly voluminous magma bodies, concluding with the highly voluminous CP (Paterson et al., 2016) as an effect of regional magma focusing (Ardill et al., 2018). Such batch-wise formation of a voluminous magma chamber has similarly been recognized in the Wooley Creek batholith in the Klamath Mountains of California (Coint et al., 2013a, 2013b). Magma focusing (i.e., increased magma body size and volumes that are regionally concentrated over a central magma plumbing system) as a system matures over time is well documented in volcanic systems from which large, commonly crystal-rich, so-called monotonous ignimbrites are erupted. Examples of such bodies include the voluminous Fish Canyon Tuff in the San Juan volcanic field in Colorado (Bachmann et al., 2002; Bachmann and Bergantz, 2003; Lipman, 2007), the tuff of the Aucanquilcha volcanic cluster in the Central Andes (Klemetti and Grunder, 2008), and the Altiplano-Puna volcanic complex in the Central Andes (de Silva and Gosnold, 2007). Even in monotonous deposits of supereruptions, such

as the Tara eruption of the Guacha II caldera in southwestern Bolivia, local compositional heterogeneities are found at hand-sample and crystal scales (Grocke et al., 2017), highlighting the similarities and parallelism found in volcanic and plutonic systems (Bachmann et al., 2007a, 2007b; Best et al., 2016). The accumulation of minerals (i.e., the "leaking" of highly evolved, siliceous melts as found in the units of the TIC and elsewhere) evidently occurred after the magmas were mixed and subsequently stored as fairly crystal-rich mushes before final crystallization. In conclusion, (1) increasing magma volumes as described by mixed feldspar populations signaling magma-body and across-unit interconnectivity and (2) the maturity of the magma plumbing system over time hold significant implications for the TIC and similar plutons recording processes associated with high-volume volcanic eruptions.

ACKNOWLEDGMENTS

Funding was provided by U.S. National Science Foundation awards EAR-1550935 and EAR-1624854 to Memeti and EAR-1550969 to Barnes. Oppenheim acknowledges funding from a Geological Society of America graduate student research grant for the use of LA-ICP-MS in acquiring trace element data. The use of the EMPA and LA-ICP-MS in Mainz, Germany, was supported by a Max-Planck Institute for Chemistry research scholarship to Krause. Thanks to Drs. Melanie Barnes and Kevin Werts for help with the acquisition of trace element data with LA-ICP-MS at Texas Tech University in Lubbock, Texas, and to Kevin Werts, Cullen Scheland, and Katie Ardill for helpful discussions about data and interpretations. We thank Drs. Ewa Słaby and Erik Klemetti for their thoughtful and constructive reviews, and Science Editor Dr. Shan de Silva and Guest Associate Editor Dr. Jonathan Miller for their helpful comments and efficient handling of the manuscript. We also thank Dr. Calvin Miller for his inspirational studies on magmatic systems.

REFERENCES CITED

Ague, J.J., and Brimhall, G.H., 1988, Regional variations in bulk chemistry, mineralogy, and the compositions of mafic and accessory minerals in the batholiths of California: Geological Society of America Bulletin, v. 100, p. 912–927, https://doi.org/10.1130/0016-7606(1988)100<0912:MAAADO>2.3.CO;2.

Annen, C., 2009, From plutons to magma chambers: Thermal constraints on the accumulation of eruptible silicic magma in the upper crust: Earth and Planetary Science Letters, v. 284, p. 409–416, https://doi.org/10.1016/j.epsl.2009.05.006.

Ardill, K., Paterson, S., and Memeti, V., 2018, Spatiotemporal magmatic focusing in upper-mid crustal plutons of the Sierra Nevada arc: Earth and Planetary Science Letters, v. 498, p. 88–100, https://doi.org/10.1016/j.epsl.2018.06.023.

Bachmann, O., and Bergantz, G.W., 2003, Rejuvenation of the Fish Canyon magma body: A window into the evolution of large-volume silicic magma systems: Geology, v. 31, p. 789–792, https://doi.org/10.1130/G19764.1.

Bachmann, O., and Bergantz, G.W., 2006, Gas percolation in upper-crustal silicic crystal mushes as a mechanism for upward heat advection and rejuvenation of near-solidus magma bodies: Journal of Volcanology and Geothermal Research, v. 149, p. 85–102, https://doi.org/10.1016/j.jvolgeores.2005.06.002.

Bachmann, O., Dungan, M.A., and Lipman, P.W., 2002, The Fish Canyon magma body, San Juan volcanic field, Colorado: Rejuvenation and eruption of an upper-crustal batholith: Journal of Petrology, v. 43, p. 1469–1503, https://doi.org/10.1093/petrology/43.8.1469.

Bachmann, O., Charlier, B.L.A., and Lowenstern, J.B., 2007a, Zircon crystallization and recycling in the magma chamber of the rhyolitic Kos Plateau Tuff (Aegean arc): Geology, v. 35, p. 73–76, https://doi.org/10.1130/G23151A.1.

Bachmann, O., Miller, C.F., and de Silva, S.L., 2007b, The volcanic–plutonic connection as a stage for understanding crustal magmatism: Journal of Volcanology and Geothermal Research, v. 167, p. 1–23, https://doi.org/10.1016/j.jvolgeores.2007.08.002.

Barnes, C.G., Ernst, W.G., Berry, R., and Tsujimori, T., 2016a, Petrology and geochemistry of an upper crustal pluton: A view into crustal-scale magmatism during arc to retro-arc transition: Journal of Petrology, v. 57, p. 1361–1388, https://doi.org/10.1093/petrology/egw043.

Barnes, C.G., Memeti, V., and Coint, N., 2016b, Deciphering magmatic processes in calc-alkaline plutons using trace element zoning in hornblende: American Mineralogist, v. 101, p. 328–342, https://doi.org/10.2138/am-2016-5383.

Barnes, C.G., Werts, K., Memeti, V., and Ardill, K., 2019, Most granitoid rocks are cumulates: Deductions from hornblende compositions and zircon saturation: Journal of Petrology, v. 60, p. 2227–2240, https://doi.org/10.1093/petrology/egaa008.

Bartley, J.M., Coleman, D.S., and Glazner, A.F., 2008, Incremental pluton emplacement by magmatic crack-seal: Earth and Environmental Science Transactions of the Royal Society of Edinburgh, v. 97, p. 383–396, https://doi.org/10.1017/S0263593300001528.

Bartley, J.M., Glazner, A.F., and Coleman, D.S., 2018, Dike intrusion and deformation during growth of the Half Dome pluton, Yosemite National Park, California: Geosphere, v. 14, p. 1283–1297, https://doi.org/10.1130/GES01458.1.

Bateman, P C., 1983, Geologic map of the Tuolumne Meadows quadrangle, Yosemite National Park, California: Geologic Quadrangle 1570, U.S. Geological Survey, https://doi.org/10.3133/gq1570.

Bateman, P.C., and Chappell, B.W., 1979, Crystallization, fractionation, and solidification of the Tuolumne intrusive series, Yosemite National Park, California: Geological Society of America Bulletin, v. 90, p. 465–482, https://doi.org/10.1130/0016-7606(1979)90<465:CFASOT>2.0.CO;2.

Best, M.G., Christiansen, E.H., de Silva, S., and Lipman, P.W., 2016, Slab-rollback ignimbrite flareups in the southern Great Basin and other Cenozoic American arcs: A distinct style of volcanism: Geosphere, v. 12, p. 1097–1135, https://doi.org/10.1130/GES01285.1.

Caricchi, L., and Blundy, J., 2015, Experimental petrology of monotonous intermediate magmas, *in* Caricchi, L., and Blundy, J.D., eds., Chemical, Physical and Temporal Evolution of Magmatic Systems: Geological Society of London Special Publication 422, p. 105–130, https://doi.org/10.1144/SP422.9.

Challener, S.C., and Glazner, A.F., 2017, Igneous or metamorphic? Hornblende phenocrysts as greenschist facies reaction cells in the Half Dome Granodiorite, California: American Mineralogist, v. 102, p. 436–444, https://doi.org/10.2138/am-2017-5864.

Chambers, M., Memeti, V., Eddy, M.P., and Schoene, B., 2020, Half a million years of magmatic history recorded in a K-feldspar megacryst of the Tuolumne Intrusive Complex, California: Geology, v. 48, p. 400–404, https://doi.org/10.1130/G46873.1.

Cherniak, D.J., 2002, Ba diffusion in feldspar: Geochimica et Cosmochimica Acta, v. 66, p. 1641–1650, https://doi.org/10.1016/S0016-7037(01)00866-3.

Cherniak, D.J., 2010, Cation diffusion in feldspar, *in* Zhang, Y.X., and Cherniak, D.J., eds., Diffusion in Minerals and Melts: Reviews in Mineralogy and Geochemistry, v. 72, p. 691–734, https://doi.org/10.1515/9781501508394-016.

Coint, N., Barnes, C.G., Yoshinobu, A.S., Barnes, M.A., and Buck, S., 2013a, Use of trace element abundances in augite and hornblende to determine the size, connectivity, timing, and evolution of magma batches in a tilted batholith: Geosphere, v. 9, p. 1747–1765, https://doi.org/10.1130/GES00931.1.

Coint, N., Barnes, C.G., Yoshinobu, A.S., Chamberlain, K.R., and Barnes, M.A., 2013b, Batch-wise assembly and zoning of a tilted calc-alkaline batholith: Field relations, timing, and compositional variation: Geosphere, v. 9, p. 1729–1746, https://doi.org/10.1130/GES00930.1.

Coleman, D.S., Gray, W., and Glazner, A.F., 2004, Rethinking the emplacement and evolution of zoned plutons: Geochronologic evidence for incremental assembly of the Tuolumne Intrusive Suite: California Geology, v. 32, p. 433–436, https://doi.org/10.1130/G20220.1.

Coleman, D.S., Bartley, J.M., Glazner, A.F., and Pardue, M.J., 2012, Is chemical zonation in plutonic rocks driven by changes in source magma composition or shallow-crustal differentiation?: Geosphere, v. 8, p. 1568–1587, https://doi.org/10.1130/GES00798.1.

Davidson, J.P., Morgan, D.J., Charlier, B.L.A., Harlou, R., and Hora, J.M., 2007, Microsampling and isotopic analysis of igneous rocks: Implications for the study of magmatic systems: Annual Review of Earth and Planetary Sciences, v. 35, p. 273–311, https://doi.org/10.1146/annurev.earth.35.031306.140211.

De Campos, C.P., Dingwell, D.B., Perugini, D., Civetta, L., and Fehr, T.K., 2008, Heterogeneities in magma chambers: Insights from the behavior of major and minor elements during mixing experiments with natural alkaline melts: Chemical Geology, v. 256, p. 131–145, https://doi.org/10.1016/j.chemgeo.2008.06.034.

de Silva, S.L., and Gosnold, W.D., 2007, Episodic construction of batholiths: Insights from the spatiotemporal development of an ignimbrite flare-up: Journal of Volcanology and Geothermal Research, v. 167, p. 320–335, https://doi.org/10.1016/j.jvolgeores.2007.07.015.

Economos, R.C., Memeti, V., Paterson, S.R., Miller, J.S., Erdmann, S., and Žák, J., 2009, Causes of compositional diversity in a lobe of the Half Dome granodiorite, Tuolumne Batholith, Central Sierra Nevada, California: Earth and Environmental Science Transactions of the Royal Society of Edinburgh, v. 100, p. 173–183, https://doi.org/10.1017/S1755691009016065.

Esposito, R., Badescu, K., Steele-Macinnis, M., Cannatelli, C., De Vivo, B., Lima, A., Bodnar, R.J., and Manning, C.E., 2018, Magmatic evolution of the Campi Flegrei and Procida volcanic fields, Italy, based on interpretation of data from well-constrained melt inclusions: Earth-Science Reviews, v. 185, p. 325–356, https://doi.org/10.1016/j.earscirev.2018.06.003.

Gelman, S.E., Gutierrez, F.J., and Bachmann, O., 2013, On the longevity of large upper crustal silicic magma reservoirs: Geology, v. 41, p. 759–762, https://doi.org/10.1130/G34241.1.

Ginibre, C., Wörner, G., and Kronz, A., 2002, Minor- and trace-element zoning in plagioclase: Implications for magma chamber processes at Parinacota volcano, northern Chile: Contributions to Mineralogy and Petrology, v. 143, p. 300–315, https://doi.org/10.1007/s00410-002-0351-z.

Glazner, A.F., and Johnson, B.R., 2013, Late crystallization of K-feldspar and the paradox of megacrystic granites: Contributions to Mineralogy and Petrology, v. 166, p. 777–799, https://doi.org/10.1007/s00410-013-0914-1.

Glazner, A.F., Bartley, J.M., Coleman, D.S., Gray, W., and Taylor, R.Z., 2004, Are plutons assembled over millions of years by amalgamation from small magma chambers?: GSA Today, v. 14, no. 4/5, p. 4–12, https://doi.org/10.1130/1052-5173(2004)014<0004:APAOMO>2.0.CO;2.

Gray, W., Glazner, A.F., Coleman, D.S., and Bartley, J.M., 2008, Long-term geochemical variability of the Late Cretaceous Tuolumne intrusive suite, central Sierra Nevada, California, *in* Annen, C., and Zellmer, G.F., eds., Dynamics of Crustal Magma Transfer, Storage and Differentiation: Geological Society of London Special Publication 304, p. 183–201, https://doi.org/10.1144/SP304.10.

Grocke, S.B., de Silva, S.L., Iriarte, R., Lindsay, J.M., and Cottrell, E., 2017, Catastrophic caldera-forming (CCF) monotonous silicic magma reservoirs: Geochemical and petrological constraints on heterogeneity, magma dynamics, and eruption dynamics of the 3.49 Ma Tara supereruption, Guacha II Caldera, SW Bolivia: Journal of Petrology, v. 58, p. 227–260, https://doi.org/10.1093/petrology/egx012.

Huber, N.K., Bateman, P.C., and Wahrhaftig, C., 1989, Geologic map of Yosemite National Park and vicinity, California: U.S. Geological Survey Miscellaneous Investigations Series Map I-1874, https://doi.org/10.3133/i1874.

Iveson, A.A., Rowe, M.C., Webster, J.D., and Neill, O.K., 2018, Amphibole-, clinopyroxene- and plagioclase-melt partitioning of trace and economic metals in halogen-bearing rhyodacitic melts: Journal of Petrology, v. 59, p. 1579–1604, https://doi.org/10.1093/petrology/egy072.

Jochum, K.P., Stoll, B., Herwig, K., and Willbold, M., 2006, Improvement of in situ Pb isotope analysis by LA-ICP-MS using a 193 nm Nd:YAG laser: Journal of Analytical Atomic Spectrometry, v. 21, p. 666–675, https://doi.org/10.1039/b603890e.

Jochum, K.P., Stoll, B., Herwig, K., and Willbold, M., 2007, Validation of LA-ICP-MS trace element analysis of geological glasses using a new solid-state 193 nm Nd:YAG laser and matrix-matched calibration: Journal of Analytical Atomic Spectrometry, v. 22, p. 112–121, https://doi.org/10.1039/B609547J.

Johannes, W., 1984, Beginning of melting in the granite system Qz-Or-Ab-An-H_2O: Contributions to Mineralogy and Petrology, v. 86, no. 3, p. 264–273.

Johnson, B.R., and Glazner, A.F., 2010, Formation of K-feldspar megacrysts in granodioritic plutons by thermal cycling and late-stage textural coarsening: Contributions to Mineralogy and Petrology, v. 159, p. 599–619, https://doi.org/10.1007/s00410-009-0444-z.

Johnson, D.M., Hooper, P.R., and Conrey, R.M., 1999, XRF analysis of rocks and minerals for major and trace elements on a single low dilution Li-tetraborate fused bead: Advances in X-Ray Analysis, v. 41, p. 843–867.

Kistler, R.W., and Fleck, R.J., 1994, Field guide for a transect of the central Sierra Nevada, California: Geochronology and isotope geology: U.S. Geological Survey Open-File Report 94-267, 50 p., https://doi.org/10.3133/ofr94267.

Kistler, R.W., Chappell, B.W., Peck, D.L., and Bateman, P.C., 1986, Isotopic variation in the Tuolumne intrusive suite, central Sierra Nevada, California: Contributions to Mineralogy and Petrology, v. 94, p. 205–220, https://doi.org/10.1007/BF00592937.

Klemetti, E.W., and Grunder, A.L., 2008, Volcanic evolution of Volcán Aucanquilcha: A long-lived dacite volcano in the Central Andes of northern Chile: Bulletin of Volcanology, v. 70, p. 633–650, https://doi.org/10.1007/s00445-007-0158-x.

Kretz, R., 1983, Symbols for rock-forming minerals: American Mineralogist, v. 68, p. 277–279.

Lipman, P.W., 2007, Incremental assembly and prolonged consolidation of Cordilleran magma chambers: Evidence from the Southern Rocky Mountain volcanic field: Geosphere, v. 3, p. 42–70, https://doi.org/10.1130/GES00061.1.

Marshall, J.D., 1988, Cathodoluminescence of Geological Materials: Unwin Hyman, 146 p.

Matzel, J.E.P., Bowring, S.A., and Miller, R.B., 2006, Time scales of pluton construction at differing crustal levels: Examples from the Mount Stuart and Tenpeak intrusions, North Cascades, Washington: Geological Society of America Bulletin, v. 118, p. 1412–1430, https://doi.org/10.1130/B25923.1.

McNulty, B.A., Tobisch, O.T., Cruden, A.R., and Gilder, S., 2000, Multistage emplacement of the Mount Givens pluton, central Sierra Nevada batholith, California: Geological Society of America Bulletin, v. 112, p. 119–135, https://doi.org/10.1130/0016-7606(2000)112<119:MEOTMG>2.0.CO;2.

Memeti, V., Paterson, S., Matzel, J., Mundil, R., and Okaya, D., 2010, Magmatic lobes as "snapshots" of magma chamber growth and evolution in large, composite batholiths: An example from the Tuolumne intrusion, Sierra Nevada, California: Geological Society of America Bulletin, v. 122, p. 1912–1931, https://doi.org/10.1130/B30004.1.

Memeti, V., Paterson, S., and Mundil, R., 2014, Day 4: Magmatic evolution of the Tuolumne Intrusive Complex, *in* Memeti, V., Paterson, S.R., and Putirka, K.D., eds., Formation of the Sierra Nevada Batholith: Magmatic and Tectonic Processes and Their Tempos: Geological Society of America Field Guide 34, p. 43–74, https://doi.org/10.1130/2014.0034(04).

Middlemost, E.A.K., 1994, Naming materials in the magma/igneous rock system: Earth-Science Reviews, v. 37, p. 215–224, https://doi.org/10.1016/0012-8252(94)90029-9.

Miller, C.F., Furbish, D.J., Walker, B.A., Claiborne, L.L., Koteas, G.C., Bleick, H.A., and Miller, J.S., 2011, Growth of plutons by incremental emplacement of sheets in crystal-rich host: Evidence from Miocene intrusions of the Colorado River region, Nevada, USA: Tectonophysics, v. 500, p. 65–77, https://doi.org/10.1016/j.tecto.2009.07.011.

Miller, J.S., Matzel, J.E., Miller, C.F., Burgess, S.D., and Miller, R.B., 2007, Zircon growth and recycling during the assembly of large, composite arc plutons: Journal of Volcanology and Geothermal Research, v. 167, p. 282–299, https://doi.org/10.1016/j.jvolgeores.2007.04.019.

Miller, R.B., and Paterson, S.R., 1999, In defense of magmatic diapirs: Journal of Structural Geology, v. 21, p. 1161–1173, https://doi.org/10.1016/S0191-8141(99)00033-4.

Miller, R.B., and Paterson, S.R., 2001, Construction of mid-crustal sheeted plutons: Examples from the North Cascades, Washington: Geological Society of America Bulletin, v. 113, p. 1423–1442, https://doi.org/10.1130/0016-7606(2001)113<1423:COMCSP>2.0.CO;2.

Moore, J.G., and Sisson, T.W, 2008, Igneous phenocrystic origin of K-feldspar megacrysts in granitic rocks from the Sierra Nevada batholith: Geosphere, v. 4, p. 387–400, https://doi.org/10.1130/GES00146.1.

Padilla, A.J., and Gualda, G.A.R., 2016, Crystal-melt elemental partitioning in silicic magmatic systems: An example from the Peach Spring Tuff high-silica rhyolite, Southwest USA: Chemical Geology, v. 440, p. 326–344, https://doi.org/10.1016/j.chemgeo.2016.07.004.

Paterson, S.R., 2009, Magmatic tubes, pipes, troughs, diapirs, and plumes: Late-stage convective instabilities resulting in compositional diversity and permeable networks in crystal-rich magmas of the Tuolumne batholith, Sierra Nevada, California: Geosphere, v. 5, p. 496–527, https://doi.org/10.1130/GES00214.1.

Paterson, S.R., and Fowler, T.K., Jr., 1993, Extensional pluton-emplacement models: Do they work for large plutonic complexes?: Geology, v. 21, p. 781–784, https://doi.org/10.1130/0091-7613(1993)021<0781:EPEMDT>2.3.CO;2.

Paterson, S.R., and Vernon, R.H., 1995, Bursting the bubble of ballooning plutons: A return to nested diapirs emplaced by multiple processes: Geological Society of America Bulletin, v. 107, p. 1356–1380, https://doi.org/10.1130/0016-7606(1995)107<1356:BTBOBP>2.3.CO;2.

Paterson, S.R., Okaya, D., Memeti, V., Economos, R., and Miller, R.B., 2011, Magma addition and flux calculations of incrementally constructed magma chambers in continental margin arcs: Combined field, geochronologic, and thermal modeling studies: Geosphere, v. 7, p. 1439–1468, https://doi.org/10.1130/GES00696.1.

Paterson, S., Memeti, V., Mundil, R., and Žák, J., 2016, Repeated, multiscale, magmatic erosion and recycling in an upper-crustal pluton: Implications for magma chamber dynamics and magma volume estimates: American Mineralogist, v. 101, p. 2176–2198, https://doi.org/10.2138/am-2016-5576.

Perugini, D., Poli, G., and Gatta, G.D., 2002, Analysis and simulation of magma mixing processes in 3D: Lithos, v. 65, p. 313–330, https://doi.org/10.1016/S0024-4937(02)00198-6.

Perugini, D., Poli, G., and Mazzuoli, R., 2003, Chaotic advection, fractals and diffusion during mixing of magmas: Evidence from lava flows: Journal of Volcanology and Geothermal Research, v. 124, p. 255–279, https://doi.org/10.1016/S0377-0273(03)00098-2.

Perugini, D., De Campos, C.P., Dingwell, D.B., Petrelli, M., and Poli, G., 2008, Trace element mobility during magma mixing: Preliminary experimental results: Chemical Geology, v. 256, p. 146–157, https://doi.org/10.1016/j.chemgeo.2008.06.032.

Ratschbacher, B.C., Keller, C.B., Schoene, B., Paterson, S.R., Anderson, J.L., Okaya, D., Putirka, K., and Lippoldt, R., 2018, A new workflow to assess emplacement duration and melt residence time of compositionally diverse magmas emplaced in a sub-volcanic reservoir: Journal of Petrology, v. 59, p. 1787–1809, https://doi.org/10.1093/petrology/egy079.

Samperton, K.M., Schoene, B., Cottle, J.M., Keller, C.B., Crowley, J.L., and Schmitz, M.D., 2015, Magma emplacement, differentiation and cooling in the middle crust: Integrated zircon geochronological–geochemical constraints from the Bergell Intrusion, Central Alps: Chemical Geology, v. 417, p. 322–340, https://doi.org/10.1016/j.chemgeo.2015.10.024.

Schaltegger, U., Brack, P., Ovtcharova, M., Peytcheva, I., Schoene, B., Stracke, A., Marocchi, M., and Bargossi, G.M., 2009, Zircon and titanite recording 1.5 million years of magma accretion, crystallization and initial cooling in a composite pluton (southern Adamello batholith, northern Italy): Earth and Planetary Science Letters, v. 286, p. 208–218, https://doi.org/10.1016/j.epsl.2009.06.028.

Schleicher, J.M., and Bergantz, G.W., 2017, The mechanics and temporal evolution of an open-system magmatic intrusion into a crystal-rich magma: Journal of Petrology, v. 58, p. 1059–1072, https://doi.org/10.1093/petrology/egx045.

Schoene, B., Schaltegger, U., Brack, P., Latkoczy, C., Stracke, A., and Günther, D., 2012, Rates of magma differentiation and emplacement in a ballooning pluton recorded by U-Pb TIMS-TEA, Adamello batholith, Italy: Earth and Planetary Science Letters, v. 355, p. 162–173, https://doi.org/10.1016/j.epsl.2012.08.019.

Scruggs, M.A., and Putirka, K.D., 2018, Eruption triggering by partial crystallization of mafic enclaves at Chaos Crags, Lassen Volcanic Center, California: American Mineralogist, v. 103, p. 1575–1590, https://doi.org/10.2138/am-2018-6058.

Siégel, C., Bryan, S.E., Allen, C.M., and Gust, D.A., 2018, Use and abuse of zircon-based thermometers: A critical review and a recommended approach to identify antecrystic zircons: Earth-Science Reviews, v. 176, p. 87–116, https://doi.org/10.1016/j.earscirev.2017.08.011.

Słaby, E., Götze, J., Wörner, G., Simon, K., Wrzalik, R., and Śmigielski, M., 2008, K-feldspar phenocrysts in microgranular magmatic enclaves: A cathodoluminescence and geochemical study of crystal growth as a marker of magma mingling dynamics: Lithos, v. 105, p. 85–97, https://doi.org/10.1016/j.lithos.2008.02.006.

Słaby, E., Śmigielski, M., Domonik, A., Simon, K., and Kronz, A., 2011, Chaotic three-dimensional distribution of Ba, Rb, and Sr in feldspar megacrysts grown in an open magmatic system: Contributions to Mineralogy and Petrology, v. 162, p. 909–927, https://doi.org/10.1007/s00410-011-0631-6.

Viswanathan, K., and Brandt, K., 1980, The crystal structure of a ternary (Ba,K,Na)-feldspar and its significance: American Mineralogist, v. 65, p. 472–476.

Viswanathan, K., and Kielhorn, H.M., 1983, Al,Si distribution in a ternary (Ba,K,Na)-feldspar as determined by crystal structure refinement: American Mineralogist, v. 68, p. 122–124.

Wallace, G.S., and Bergantz, G.W., 2002, Wavelet-based correlation (WBC) of zoned crystal populations and magma mixing: Earth and Planetary Science Letters, v. 202, p. 133–145, https://doi.org/10.1016/S0012-821X(02)00762-8.

Werts, K., Barnes, C.G., Memeti, V., Ratschbacher, B., Williams, D., and Paterson, S.R., 2020, Hornblende as a tool for assessing mineral-melt equilibrium and recognition of crystal accumulation: American Mineralogist, v. 105, p. 77–91, https://doi.org/10.2138/am-2020-6972.

Žák, J., and Paterson, S.R., 2005, Characteristics of internal contacts in the Tuolumne Batholith, central Sierra Nevada, California (USA): Implications for episodic emplacement and physical processes in a continental arc magma chamber: Geological Society of America Bulletin, v. 117, p. 1242–1255, https://doi.org/10.1130/B25558.1.

Zhang, J., Davidson, J.P., Humphreys, M.C.S., Macpherson, C.G., and Neill, I., 2015, Magmatic enclaves and andesitic lavas from Mt. Lamington, Papua New Guinea: Implications for recycling of earlier-fractionated minerals through magma recharge: Journal of Petrology, v. 56, p. 2223–2256, https://doi.org/10.1093/petrology/egv071.